Intra-cluster receptor density (IRD): a molecular switch for TNFR1 clusters' signaling

Short title

TNFR1 IRD influences its downstream signaling

Authors

Subhamoy Jana[1]†, Priyanka Roy[1]†, Jibitesh Das[2], Basab Bijayee Bera[1], Parijat Biswas[1], Nandana Nanda[1], Bidisha Sinha[2], Deepak Kumar Sinha[1]*

Affiliations

[1] School of Biological Sciences, Indian Association for the Cultivation of Science; Kolkata 700032, India.

[2] Department of Biological Sciences, Indian Institute of Science Education and Research Kolkata; Mohanpur 741246, India.

* Corresponding author: Deepak Kumar Sinha

Email: bcdks@iacs.res.in , emaildks@gmail.com

† Equal first-author contribution

Abstract

Tumor Necrosis Factor Receptor 1 (TNFR1) signaling regulates cell fate in inflammation, immune responses, and tumorigenesis. While TNF-α–mediated TNFR1 pathways are well known, the role of receptor clustering remains unclear. Utilizing homo-FRET using fluorescence anisotropy, we show that intra-cluster receptor density (IRD) governs TNFR1 signaling outcomes. Soluble TNF-α (sTNF-α) increases IRD at cluster cores but decreases it at rims via receptor reorganization. Reducing IRD through membrane tension, zafirlukast, actin depolymerization, or cholesterol depletion suppresses sTNF-α signaling, whereas increasing IRD by lowering membrane tension or exposing cells in a 3D gel-like microenvironment triggers ligand-independent activation. These findings reveal IRD as a key regulator of receptor signaling, with potential relevance across related receptor families and innovative strategies in modulating TNFR1 signaling.

Teaser

Intra-cluster receptor density (IRD) is critical for TNFR1 signal modulation, with higher IRD activating and lower IRD impairing the TNFR1 signaling.

MAIN TEXT

Introduction

Tumor necrosis factor receptor 1 (TNFR1) is a type I transmembrane protein of the TNF receptor superfamily (TNFRSF) (*1*, *2*), which plays a multifaceted role in modulating numerous cellular processes, encompassing inflammation (*3*, *4*), cell survival (*5*), apoptosis (*6*, *7*), and differentiation (*8*). While TNF-α-mediated TNFR1 signaling pathways (*9*, *10*) are widely known, the role of receptor clustering in downstream signal activation remains unexplored. Studies in cell-free systems suggest that the trimeric ligand TNF-α (*11*) interacts with TNFR1s in their native monomeric and/or dimeric state (*12*) to form the trimeric TNFR1 primary cluster(*13*) , which acts as the basic signaling unit. Further, the interaction among pre-ligand assembly domains (PLAD) across different TNFR1 primary clusters promotes the formation of ligand-independent, higher-order TNFR1 secondary clusters on the cell membrane (*14–19*). Besides PLAD, TNFR1 interacts via its other domains, including cysteine-rich domains (CRDs) (*20*), transmembrane domain (TMD) (*21*), and cytoplasmic domain (CD) (*22*, *23*), assembling ligand-receptor and receptor-receptor complexes into larger clusters. Our observation, along with others, indicates that TNFR1

consistently forms pre-formed clusters on the cell membrane even without additional ligand stimulation (*18*, *22*).

Understanding the importance of TNFR1 clustering in downstream signaling is crucial for therapeutic advancements. The targeted treatment using small molecule inhibitors (**table S1**) and/or the polymorphism-induced TNFR1 dysfunctions (*24–29*) is limited, primarily focusing on ligand sequestration or decoy receptors (*30*). Thus, it highlights the need for a deeper understanding of TNFR1 cluster organization and its role in modulating downstream signaling across various conditions.

TNFR1 clustering has been studied with its ligand at basal and stimulated states (*14*), but the organization within pre-formed clusters and their impact on downstream signaling remain unclear. A previous study on TNFR1 signal activation by reinforcing secondary clusters with agonistic antibodies (*31*, *32*) suggests that an increase in receptor density within the cluster activates the signaling. In our study, we showed that the density of TNFR1 receptors within pre-formed TNFR1 clusters, referred to as intra-cluster receptor density (IRD), is a crucial determinant of its downstream signaling. We anticipated that IRD modulates signaling efficacy through cooperativity. In this context, cooperativity refers to a collective behavior in which receptor activation is influenced by the spatial proximity of neighboring receptors within a cluster, thereby modulating its likelihood of activation.

Manipulating the IRD while preserving other biochemical parameters, such as chemical composition and the biomolecular organization, is a challenging task. Using HeLa as a model system, we subjected cells to diverse conditions that alter the TNFR1 cluster's IRD to examine its link with the TNFR1 downstream signaling state. Initially, we investigated whether the activation of TNFR1 signaling by soluble TNF-α (sTNF-α) or inhibition by the antagonist zafirlukast (*33*, *34*) occur by modulating the IRD. Further, we explored other avenues that could influence IRD, namely, altered plasma membrane tension, actin depolymerization, changes in extracellular microenvironment, and cholesterol depletion on TNFR1's IRD and signaling efficacy. We used the fluorescence anisotropy-based homo-FRET technique to assess TNFR1 IRD, where loss of anisotropy reflects increased homo-FRET (*35–38*) and receptor proximity and thus, IRD. Variations in fluorescence anisotropy within TNFR1-EGFP clusters indicate differential homo-FRET efficiency, where the anisotropy map inversely correlates with the TNFR1 IRD, as elucidated in Materials and Methods.

82 The canonical NF-κB pathway is a major signaling cascade activated downstream of TNFR1,
83 promoting pro-inflammatory and pro-survival responses. Upon ligand binding, TNFR1 recruits
84 adaptor proteins, such as TNF Receptor Type 1-Associated Death Domain Protein (TRADD), TNF
85 Receptor–Associated Factor 2 (TRAF2), Receptor-Interacting Protein Kinase 1(RIPK1), and
86 Cellular Inhibitor of Apoptosis Protein 1 and 2 (cIAP1/2), via its cytoplasmic death domain to form
87 the membrane-bound Complex I. A critical step in this pathway is the ubiquitination of RIPK1 by
88 cIAP1/2, which attaches K63- and M1-linked ubiquitin chains. These chains act as platforms for
89 the recruitment of downstream signaling complexes, including Linear Ubiquitin Chain Assembly
90 Complex (LUBAC), TAK1-Binding Protein 2 and 3 (TAB2/3), Transforming Growth Factor Beta–
91 Activated Kinase 1 (TAK1), and the IκB Kinase Complex (IKK) complex (composed of IKKα,
92 IKKβ, and NF-κB Essential Modulator (NEMO)) (*39–41*). TNFR1 signal activation triggers IKK
93 phosphorylation, leading to Nuclear Factor Kappa-Light-Chain-Enhancer of Activated B Cells
94 (NF-κB (p65/p50)) nuclear translocation (*41*). We assessed the downstream signaling of TNFR1 by
95 NF-κB activation assay in different physiological conditions, which can alter the TNFR1 IRD.

96 This manuscript demonstrates that altering the TNFR1 IRD changes the response to TNF-α in
97 downstream signaling, both in a ligand-dependent and ligand-independent manner. Our findings
98 provide valuable insights into the role of clustering in TNFRSF function and its potential
99 implications for therapeutic strategies.

100 Results

101 Fluorescence anisotropy mapping reveals heterogeneous packing in TNFR1 clusters

102 We cloned human TNFR1 into the mEGFP-N1 backbone to generate a TNFR1-EGFP construct
103 (**Fig. 1A**). Immunostaining in transiently transfected HeLa cells confirmed that TNFR1-EGFP
104 assembled into membrane clusters resembling endogenous TNFR1. We designated clusters lacking
105 EGFP as "endogenous" (**fig. S1A**) and those containing EGFP as "exogenous" (**Fig. 1B and fig.**
106 **S1B**). Time-lapse imaging at 20 Hz in Total Internal Reflection Fluorescence (TIRF) mode revealed
107 exponential photobleaching of exogenous clusters, consistent with a large number of TNFR1-EGFP
108 molecules per cluster (**fig. S1C**). In contrast, clusters composed of only a few molecules are
109 expected to photo-bleach in discrete steps (*42–44*). The colocalization of EGFP and anti-TNFR1
110 (**Fig. 1B and fig. S1B**), together with sequencing validation, confirmed the construct's accuracy.
111 The fraction of TNFR1-EGFP clusters localized to the plasma membrane increased with time after
112 transfection (**fig. S1D**) reaching ~76 ± 8% by 18 hours (**Fig. 1C and movie S1**). A minority of

113 clusters displayed high mobility (**movie S2**), likely reflecting intracellular vesicles. Treatment with
114 the dynamin inhibitor dynasore (*45*) reduced the fraction of mobile clusters (**movie S3**). However,
115 a considerable number of mobile clusters remained, suggesting that they may arise from multiple
116 sources, including endocytic vesicles as well as transport vesicles carrying TNFR1-EGFP from the
117 ER, through the Golgi, to the plasma membrane.

118 Fluorescence anisotropy (r) mapping of TNFR1-EGFP clusters in live cells revealed marked intra-
119 cluster heterogeneity (**Fig. 1D**). The central core exhibited lower anisotropy ($\bar{r}_{core}$) than the outer
120 rim ($\bar{r}_{rim}$) (**Fig. 1E**), suggesting that the intra-cluster variations in r could originate from differing
121 homo-FRET efficiencies. The lower $\bar{r}_{core}$ value implies a heightened homo-FRET efficiency in the
122 core, indicating a denser packing of TNFR1 molecules in the core than in the rim or a higher IRD
123 in the core than in the rim. The anisotropy reflects the degree of polarization of the fluorescence,
124 and it decreases when emitted photons get depolarized due to factors such as molecular rotation.
125 Homo-FRET, a fluorescence resonance energy transfer between identical fluorophores in close
126 proximity, leads to such depolarization without requiring molecular rotation (*36*). This occurs
127 because the energy is transferred to a neighboring fluorophore with an unfavorably oriented
128 emission dipole, which can be established using EGFP dimers. Thus, homo-FRET is expected to
129 cause a measurable loss in anisotropy, making anisotropy a sensitive readout for detecting
130 molecular proximity and clustering of identical fluorophores. We validated this relationship by
131 comparing monomeric EGFP with EGFP dimers (2EGFP), where photobleaching-induced
132 conversion of dimers to monomers increased anisotropy (**fig. S1E**) (*46*). A similar anisotropy
133 increase occurred in TNFR1-EGFP clusters upon photobleaching (**fig. S1F**), confirming the homo-
134 FRET as the origin of intra-cluster anisotropy variations. Photobleaching produced a greater
135 anisotropy increase in the core than in the rim (**Fig. 1F**), consistent with denser packing in the core
136 (*37*, *38*). When homo-FRET was nearly eliminated, anisotropy maps became uniform (**fig. S1G**),
137 excluding the possibility of imaging or computational artifacts. To test whether higher EGFP
138 mobility at the rim influenced anisotropy, we varied linker length, but observed minimal changes
139 in $\bar{r}_{core}$ or $\bar{r}_{rim}$ (**fig. S2A**), reinforcing that anisotropy differences arise from IRD variation rather
140 than tag flexibility. Therefore, we used a 14 aa linker-length plasmid of TNFR1-EGFP in all
141 subsequent experiments unless specified otherwise.

142 We next altered receptor abundance by depleting cellular TNFR1 levels. Optimal TNFR1
143 knockdown was achieved with 30 nM siRNA over 4 days (**fig. S2B**). Immunoblotting confirmed
144 dose-dependent TNFR1-EGFP expression, plateauing at 0.5 μg plasmid (**Fig. 1G**). Knockdown

145 reduced both endogenous and exogenous TNFR1 (**Fig. 1G**), including ~30% of endogenous surface
146 receptors **(Fig. 1H**). Fluorescence anisotropy measurement revealed that TNFR1 depletion or
147 overexpression did not alter TNFR1-EGFP clusters' IRD (**Fig. 1I**). However, depletion
148 significantly reduced endogenous cluster area (**Fig. 1J**), and overexpression of TNFR1-EGFP did
149 not rescue the endogenous cluster size (**fig. S2C**). Instead, overexpression increased the size of
150 exogenous clusters in a dose-dependent manner (**Fig. 1J**), while endogenous clusters remained
151 surprisingly unaffected (**fig. S2C**). In siRNA-treated cells, TNFR1-EGFP cluster areas failed to
152 scale with plasmid dose and remained smaller than in controls (**fig. S2D**). Importantly, $\bar{r}_{core}$ and
153 $\bar{r}_{rim}$ values were independent of cluster area across all conditions (**fig. S2E**).

154 Dynamic and spontaneous rearrangement of receptor molecules occurs within TNFR1 155 clusters.

156 We examined the intra-cluster dynamics of TNFR1 molecules under physiological conditions.
157 Time-lapse anisotropy maps of TNFR1-EGFP clusters in live HeLa cells (**Fig. 2A**) revealed
158 significant temporal variations in $\bar{r}_{core}$. To ascertain that the temporal variations in $\bar{r}_{core}$ result from
159 dynamic changes in local IRD within the core and not instrumental noise, we compared the changes
160 in the cluster's $\bar{r}_{core}$ in live cells with those in fixed cells (**Fig. 2B**), and observed a significantly
161 smaller temporal variation (**Fig. 2, C and D**). We hypothesized that the crosslinking of proteins
162 hinders the intra-cluster reorganization of TNFR1-EGFP molecules. The notably lower variations
163 (±5%) of $\bar{r}_{core}$ in fixed clusters compared to live clusters (±20%) indicated that the temporal
164 variations of $\bar{r}_{core}$ in live cells, originated from a change in the local IRD due to intra-cluster
165 reorganization of receptors. The anisotropy changes in the fixed cluster (**Fig. 2D)** further suggest
166 that a change below 5% in our experimental setup could arise from measurement noise. A lack of
167 fluorescence recovery after photobleaching (FRAP) of the TNFR1-EGFP cluster (**Fig. 2E**)
168 established a negligible change in the total number of receptor molecules associated with the cluster
169 within 90-second. Furthermore, the temporal variations of $\bar{r}_{core}$ and $\bar{r}_{rim}$ were consistently higher
170 in live cells compared to fixed cells, regardless of the TNFR1-EGFP linker flexibility (**fig. S3**). This
171 suggests that the increased temporal fluctuations in anisotropy originate from dynamic intra-cluster
172 reorganization of the receptor, rather than from enhanced EGFP mobility due to linker flexibility
173 in live cells.

174 Since the intra-cluster reorganization of receptors may also alter the rim's IRD, we analyzed
175 whether our method can capture the associated temporal variations of homo-FRET in the rim.

176 Comparison of the temporal variation of relative changes in $\bar{r}_{rim}$ in live (**Fig. 2F**) to the clusters in
177 fixed (**Fig. 2G**) cells demonstrated that our experimental arrangement can monitor the changes in
178 the rim's IRD. Intra-cluster reorganization of receptors in the cluster should lead to fluorescence
179 redistribution across the cluster's core and the rim. The higher fluctuations of normalized fractional
180 intensity in the core ($F_{core}(t)$) in live (**Fig. 2H**) than in fixed (**Fig. 2I**) cells, reconfirmed intra-
181 cluster reorganization of the TNFR1-EGFP.

182 sTNF-α binding and PLAD inhibition differentially remodel TNFR1 IRD and 183 signaling

184 The continuous intra-cluster reorganization observed in TNFR1-EGFP clusters (**Fig. 2**) prompted
185 us to test whether sTNF-α binding enforces receptor rearrangement. We therefore examined
186 changes in anisotropy maps following stimulation with sTNF-α or inhibition with zafirlukast (*34*,
187 *47*). Consistent with its role in activating TNFR1, sTNF-α increased nuclear NF-κB (p65) levels
188 (*48*) with 20 ng/mL sufficient to induce maximal p65 activation within 15 minutes (**Fig. S4A**). For
189 reproducibility, nuclear translocation was quantified at 30 minutes. Within 5 minutes, sTNF-α
190 reduced TNFR1-EGFP cluster anisotropy in the core while increasing anisotropy in the rim (**Fig.
191 3, A and B**), indicating elevated IRD in the core and reduced IRD in the rim. This was accompanied
192 by a modest but significant increase in cluster area within 30 minutes (**fig. S4B**), consistent with
193 recruitment of additional receptors. These results support three hypotheses: (i) TNFR1 clusters
194 contain both ligand-bound (**fig. S4C**) and ligand-free receptors, (ii) receptor rearrangement occurs
195 on the experimental timescale, and (iii) ligand-bound receptors preferentially localize to the cluster
196 core. Consequently, due to the higher tendency of ligand-bound TNFR1s to reside in the core, rim's
197 IRD decreased upon sTNF-α addition.

198 Zafirlukast, a leukotriene receptor antagonist (*49*) that binds to the PLAD domain inhibiting TNFR1
199 PLAD-PLAD interaction, therefore it is expected to disrupt secondary clustering, effectively
200 inhibiting sTNF–α–mediated NF-κB activation (*33*, *34*, *47*) at 100 μM within 1 hour (**Fig. S4D**).
201 Unlike sTNF-α, zafirlukast caused a global reduction in IRD across both core and rim (**Fig. 3, C
202 and D**), reflected by increased anisotropy values, while preserving cluster integrity. Photobleaching
203 analysis showed that sTNF-α increased homo-FRET in the cluster core. In contrast, zafirlukast
204 markedly reduced homo-FRET in both core and rim, as indicated by changes in relative mean
205 anisotropy after 50–60% photobleaching (**Fig. 3E**). A negative correlation between initial
206 anisotropy ($\bar{r}_i$) and photobleaching-induced anisotropy changes (**Fig. 3F**) established substantial

inter-cluster IRD variation in the core. While sTNF-α minimally affected the rim, zafirlukast reduced IRD in both compartments (**Fig. 3G**), consistent with preferential localization of ligand-bound receptors in the core.

We next examined the relationship between IRD and signaling efficacy. Depletion of TNFR1 decreased the basal nuclear-to-cytoplasmic ratio of endogenous NF-κB (**fig. S4E**), indicating that basal signaling depends on receptor abundance (**Fig. 1H**). Conversely, TNFR1-EGFP overexpression **(Fig. 1G**) elevated basal NF-κB activity (**fig. S5A**), likely through increased surface receptor levels. For a given dose of sTNF-α, the increase of N/C ratio of NF-κB (**Fig. 3H and fig. S4E**), normalized to surface receptor levels in the cell, can be used as a quantitative indicator of ligand signaling efficacy. The effect of sTNF-α significantly diminished in TNFR1-depleted HeLa cells, confirming that p65 nuclear translocation is mediated through TNFR1 signaling. Zafirlukast markedly reduced sTNF-α efficacy (**Fig. 3H, and figs. S4E and S5B**) without altering surface or total TNFR1 abundance (**Fig. 3I and fig. S5C**). A slight increase in surface TNFR1 levels after 30 minutes of sTNF-α stimulation (**Fig. 3I and fig. S5D**) did not rescue signaling in the presence of zafirlukast (**Fig. 3H**). Thus, reduced signaling efficacy under zafirlukast reflects impaired IRD (**Fig. 3D**) rather than altered receptor number. Notably, NF-κB activation correlated with IRD changes-increased core IRD promoted signaling, whereas decreased IRD impeded activation (**Fig. 3, B, D, and H**). Finally, we assessed whether zafirlukast dislodged receptors from the clusters. TIRF imaging revealed a modest but significant reduction in TNFR1-EGFP cluster area (**Fig. 3J**), suggesting receptor loss, yet clusters were not fully disassembled, indicating that interactions beyond PLAD–PLAD contacts maintain structural integrity (*21*).

Membrane tension affects the TNFR1 signaling by modulating IRD

Based on our finding that the IRD of TNFR1 clusters determines their signaling state (**Figs. 2 and 3**), we next examined how membrane tension, a factor known to modulate local curvature (*50–52*) and lipid packing (*53*) influences IRD and signaling. Consequently, HeLa cells were subjected to osmotic perturbations while monitoring membrane tension with Flipper-TR (*54*). Within 2 minutes of hypotonic treatment (75% water), cells displayed elevated membrane tension (**Fig. 4A and fig. S6A**), whereas hypertonic treatment reduced membrane tension after 2 minutes (150 mM mannitol; **Fig. 4B and fig. S6B**). These changes in tension directly altered cluster IRD: hypotonic stress increased fluorescence anisotropy in both core and rim, indicating reduced IRD (**Fig. 4C**), while hypertonic stress decreased anisotropy, reflecting an increase in IRD (**Fig. 4D**). We exploited

membrane tension-induced changes in IRD (**Fig. 4, C and D**) to explore the relationship between receptor density and signaling efficiency (**Fig. 4E and fig. S6C**). The decrease in IRD under hypotonic stress resembled that seen with zafirlukast treatment (**fig. S6D**). Functionally, reduced IRD (**Fig. 4C**) did not independently trigger NF-κB translocation (**Fig. 4E**), whereas elevated IRD under hypertonic stress induced p65 translocation, even if less efficiently than sTNF-α stimulation (**Fig. 4E**). Western blot analysis of phosphorylated p65 further confirmed that sTNF-α failed to activate p65 under hypotonic conditions (**fig. S6E**). Importantly, NF-κB translocation was abolished in TNFR1-depleted cells (**Fig. 4E**), demonstrating that hypertonicity-induced activation of NF-κB is TNFR1-dependent. As no external sTNF-α was supplied, we conclude that TNFR1 activation occurred independently of sTNF-α stimulation.

We next compared the response to exogenous sTNF-α under altered tension. While surface TNFR1 was reduced under hypotonic conditions, hypertonicity caused negligible changes (**Fig. 4F**), and total cellular TNFR1 levels remained unchanged across conditions **(fig. S5C**). Strikingly, sTNF-α failed to induce NF-κB nuclear translocation in hypotonic conditions **(Fig. 4G and fig. S6E**), consistent with suppressed signaling under reduced IRD. In contrast, hypertonic stress not only promoted ligand-free TNFR1 activation but also enhanced the response to sTNF-α, as confirmed by increased p65 phosphorylation (**Fig. 4G and fig. S6E**). Quantification revealed that signaling efficacy dropped sharply under hypotonic conditions, but only modestly under hypertonic conditions (**Fig. 4H).**

Finally, we examined the morphological changes in clusters using TIRF imaging. Hypotonic stress caused a small but significant decrease in TNFR1-EGFP cluster (**Fig. 4I and fig. S6F**), suggesting receptor loss from clusters. In contrast, hypertonicity had minimal effect on cluster area (**fig. S6G**). Together, these results indicate that increased membrane tension reduces cluster IRD and partial receptor dissociation, thereby impairing TNFR1 signaling, whereas decreased tension increases IRD and supports ligand-free receptor activation.

Mechanical cues from a 3D gel-like microenvironment trigger TNFR1 signaling independent of ligand

Our previous work showed that transitioning THP-1 monocytes from a fluid-like 2D to a gel-like 3D extracellular microenvironment induces ligand-free NF-κB activation and differentiation into macrophages (*55*). To test whether TNFR1 mediates this response, we embedded HeLa cells in a 3D gel-like matrix. Similar to THP-1 cells, HeLa cells exhibited sTNF-α–independent nuclear

translocation of NF-κB, as observed both with p65-EGFP (**fig. S7, A and B**) and by immunostaining of endogenous p65 (**Fig. 5A and fig. S7C**). TNFR1 inhibition (**fig. S7, A, B and C**) or depletion (**Fig. 5A**) abolished nuclear translocation of endogenous NF-κB and p65-EGFP in a 3D gel-like extracellular microenvironment, confirming that microenvironment-mediated NF-κB activation requires TNFR1. Notably, this activation occurred without changes in TNFR1 surface levels (**fig. S7D**).

We next examined how a 3D microenvironment influenced IRD. In contrast to sTNF-α, which increased IRD in the core and reduced it in the rim (**Fig. 3B**), or osmotic perturbations, which altered both regions in the same direction (**Fig. 5C**), the 3D gel-like condition increased IRD simultaneously in both the core and rim (**Fig. 5B**). This effect was blocked by zafirlukast, linking IRD changes to TNFR1 signaling (**Fig. 5C)**. Because same-directional IRD changes in core and rim are indicative of altered membrane tension, we hypothesized that a 3D matrix lowers membrane tension. Consistent with this, cells transitioning from 2D to 3D gradually exhibited higher IRD in both core and rim (**Fig. 5D**), while Flipper-TR lifetime measurements confirmed reduced membrane tension in both HeLa (**Fig. 5E**) and THP-1 cells (**fig. S7E**). Reversing cells from 3D back to 2D restored IRD within 15 minutes (**Fig. 5F**), indicating tension-dependent reversibility of the IRD.

Structurally, the 3D microenvironment increased TNFR1-EGFP cluster area (**Fig. 5G),** but no correlation was found between cluster size and IRD **(Fig. 5H and fig. S7F).** Together, these findings suggest that 3D gel-like environments activate TNFR1 signaling in a ligand-independent manner by reducing membrane tension and increasing IRD across the cluster in addition to increasing its size.

Structural integrity of actin and cholesterol is essential for TNFR1 signaling

Given the role of the cytoskeleton in membrane organization and receptor signaling, we next tested whether actin integrity affects TNFR1 clustering and signaling. Disruption of actin filaments with cytochalasin D (CytoD) did not alter surface TNFR1 levels (**Fig. 6A**) or total TNFR1 abundance (**fig. S5C**), but it reduced IRD in both the core and rim of clusters **(Fig. 6B**). Functionally, CytoD induced NF-κB translocation even in TNFR1-depleted cells (**Fig. 6C and fig. S8A)**, consistent with reports that CytoD activates NF-κB through ROS generation (*56*). Indeed, the ROS quencher vitamin C (**fig. S8B**) (*57–59*) abolished CytoD-induced NF-κB nuclear translocation (**fig. S8, C and D)** without affecting cluster IRD (**fig. S8E**). Notably, vitamin C had no impact on sTNF-α–

300 induced NF-κB activation in untreated cells (**fig. S8, C and D**). When comparing signaling kinetics,
301 CytoD-treated cells exhibited delayed NF-κB translocation in response to sTNF-α relative to
302 control cells (**Fig. 6D**), consistent with reduced IRD impairing TNFR1 signaling efficiency.

303 We next investigated whether membrane cholesterol, another key determinant of receptor
304 organization (*60*), influences TNFR1 clustering and signaling. Cholesterol depletion with methyl-
305 β-cyclodextrin (MβCD) significantly reduced IRD in TNFR1 clusters (**Fig. 6E**), likely through
306 elevated membrane tension (**Fig. 6F**) (*61*) and/or direct effects on clustering (*60*). Cholesterol
307 depletion caused negligible changes in cluster area (**fig. S9A**) and did not affect surface TNFR1
308 levels (**Fig. 6A**), suggesting that receptor loss from clusters was minimal. Despite preserved
309 receptor abundance, cholesterol depletion impaired sTNF-α–mediated NF-κB activation (**Fig. 6G**
310 **and fig. S9B**). Together, these findings demonstrate that both actin disruption and cholesterol
311 depletion reduce TNFR1 IRD without significantly altering receptor abundance, thereby
312 diminishing the signaling efficacy of TNFR1 clusters in response to sTNF-α (**Fig. 6H**).

313 **Discussion**

314 Clustering of transmembrane receptors is a conserved mechanism for initiating signaling across
315 diverse systems, including receptor tyrosine kinases (*44*, *62*), T-cell receptors (*63*), bacterial
316 chemoreceptors (*64*), and TNFRs (*1*, *14*). In the TNFR superfamily, ligand-bound TNF–TNFR
317 trimers pre-assemble into higher-order clusters (*22*) where the extracellular PLAD domain
318 organizes into a hexagonal lattice (**Fig. 7 and fig. S4C)** (*65*, *66*).

319 On the cytoplasmic side of TNFR1, the death domain is connected to the membrane by a long,
320 flexible 122–amino acid loop (>41 nm), followed by an additional 17–amino acid loop (5.8 nm) at
321 the C-terminus (Uniprot ID: P19438). To visualize receptor organization, we inserted an extra
322 linker (7–21 amino acids; 2.4-7.1 nm) between TNFR1 and the EGFP tag. The extended
323 cytoplasmic loops together with the engineered flexible linkers are therefore expected to provide
324 high conformational flexibility to the EGFP tag. Instead of aligning with the ordered extracellular
325 PLAD lattice, the tags likely adopt variable positions and orientations, producing heterogeneous
326 EGFP distributions within TNFR1 nanoclusters (**Fig. 1, D and I, and Fig. 7**).

327 In our study, the nuclear translocation of NF-κB served as an indicator of TNFR1 signal activation.
328 Stimulation with sTNF-α induces rapid NF-κB activation, with p65 nuclear translocation observed
329 within five minutes (**fig. S4A and Fig. 6D**), even though surface-level TNFR1s remain unchanged

during this time (**fig. S5D**). Subtle increases in cluster size appear only after 30 minutes of stimulation (**fig. S4B**), suggesting that local receptor reorganization—rather than cluster enlargement—is the primary trigger for signaling. This is supported by the rapid increase in IRD detected within five minutes of sTNF-α stimulation (**Fig. 3, A and B**). Manipulating TNFR1 expression further supports the role of clustering in signaling output: overexpression of TNFR1–EGFP enlarges exogenous cluster size (**fig. 1J**) and enhances p65 nuclear translocation (**fig. S5A**), whereas TNFR1 knockdown reduces endogenous and exogenous cluster size and lowers basal NF-κB activity (**Fig. 1J, fig. S2D, and fig. S4E**). Surface levels of TNFR1-EGFP could not be directly measured by FACS because the anti-TNFR1 antibody detects both exogenous and endogenous receptors. Together, these results indicate that TNFR1 signaling is governed by both IRD and cluster size, with IRD serving as the more sensitive determinant.

To quantify IRD, we used homo-FRET as a readout of IRD by measuring steady-state fluorescence anisotropy of TNFR1-EGFP, which offers advantages for homo-oligomeric receptors by avoiding stoichiometric imbalances seen with hetero-FRET measurements (*67*). The FRET efficiency is strongly dependent on the proximity of the receptors (2-10 nm), therefore making homo-FRET a good indicator of IRD changes. A negative correlation between anisotropy and photobleaching-induced FRET recovery confirmed that anisotropy maps reflect IRD distribution (**Fig. 1F and Fig. 3F**). Importantly, IRD was largely unaffected by variations in TNFR1 expression (**Fig. 1I**), confirming that our measurements were not biased by overexpression artifacts and supporting the cluster size-dependent activation. Our data reveal that TNFR1 clusters are highly dynamic, with receptors undergoing spontaneous intra-cluster rearrangement (**Fig. 2**). We suggest that the spontaneous intra-cluster reorganization of TNFR1 clusters, together with available vacant ligand-binding sites, enables a signaling output that scales with the dose of soluble TNF-α (**fig. S4A**). Thus, ligand stimulation further reorganizes receptors within clusters to modulate IRD in the core (**Fig. 3, A and B**). Pharmacological reduction of IRD with zafirlukast (**Fig. 3, C and D**) decreased cluster size (**Fig. 3J**) without altering surface receptor levels (**Fig. 3I**), demonstrating that IRD modulation is sufficient to regulate TNFR1 signaling state (**Fig. 3H**). Physical perturbations of the membrane microenvironment also modulate IRD. Hypertonic, hypotonic, and 3D agarose environments, which alter membrane tension, significantly shifted IRD. To independently determine the changes associated with membrane tension, we used the mechanosensitive probe Flipper-TR, which reports on variations in lipid order packaging under hypotonic (**Fig. 4A and fig. S6A**), hypertonic (**Fig. 4B and fig. S6B**), and 3D environments (**Fig. 5E and fig. S7E**). Disruption of actin filaments with cytochalasin D reduced IRD in both the core and rim of TNFR1 clusters and

delayed NF-κB translocation in response to sTNF-α. This indicates that actin integrity is important for maintaining optimal TNFR1 cluster organization and signaling output. Similarly, cholesterol depletion using MβCD decreased IRD and impaired sTNF-α-mediated NF-κB activation, without significantly altering receptor abundance or cluster area. These results suggest that membrane cholesterol contributes to the structural organization of TNFR1 clusters and thereby modulates signaling efficacy. Since MβCD directly alters lipid composition by depleting membrane cholesterol (*68*), we instead relied on interference reflection microscopy (IRM) to assess membrane tension under cholesterol depletion (**Fig. 6F)** (*69*). Increased IRD led to ligand-independent activation of TNFR1 signaling, whereas decreased IRD rendered clusters unresponsive to sTNF-α, indicating that IRD functions as a molecular switch controlling signaling competence. In a hypertonic condition, the increase in IRD is accompanied by a negligible change in cluster size (**fig. S6G**) and surface level of receptors (**Fig. 4F**), strongly suggesting ligand-independent and IRD-mediated TNFR1 activation. Interestingly, hypertonic stress induced p65 nuclear translocation without detectable Ser536 phosphorylation (**fig. S6E**), implying activation through alternative p65 modifications (*70*). We also note an apparent increase in fluorescence intensity and the number of visible clusters under hypertonic conditions (**fig. S6G**). However, given the short exposure period, such an effect is unlikely to reflect a genuine rise in receptor abundance. Flow cytometry confirmed unchanged surface TNFR1 levels (**Fig. 4F**). We attribute this apparent rise to an increase in the penetration depth of the TIRF evanescent field due to refractive index changes in the hypertonic medium and to the cell shrinkage that likely brings cytoplasmic clusters closer to the membrane, making them detectable in TIRF imaging (**fig. S6G**).

We also addressed potential methodological concerns regarding EGFP tagging and anisotropy measurements. The use of monomeric EGFP connected by long flexible loops and a linker minimized steric hindrance and orientation artifacts, and functional assays confirmed signaling competence (**fig. S5A**). In conclusion, we demonstrate that IRD is a critical determinant of TNFR1 signaling, capable of modulating receptor activity independently of ligand binding. Our findings highlight IRD as a biophysical parameter that integrates membrane environment, receptor expression, and cytoskeletal architecture to fine-tune TNFR1-mediated NF-κB activation. This approach provides a framework for studying clustering-dependent regulation of other receptors and may have implications for pathological conditions where receptor clustering is dysregulated.

395 ## Materials and Methods

396 ### Plasmids

397 The following plasmids were obtained from Addgene: pTNFR1-tdEOS, a contribution from Mike
398 Heilemann (#98273); mEGFP-N1, provided by Michael Davidson (#54767); and EGFP-p65, gifted
399 by Johannes A. Schmid (#111190). The 2GFP (GFP-GFP) plasmid was generously provided by
400 Prof. Maria Vartiainen from the University of Helsinki, Finland. The TNFR1-EGFP plasmid was
401 constructed by sub-cloning the TNFR1 gene from the pTNFR1-tdEOS plasmid into the N-terminal
402 of the mEGFP-N1 plasmid, with a flexible linker of 14 amino acids in between. The full-length
403 human TNFR1 gene sequence was amplified by polymerase chain reaction (PCR) using the
404 following primers:

405 5'-cggagctc**gccacc**ATGGGCCTCTCCACCGTGCCTG-3' (forward)

406 5'-gtgtcgactcTCTGAGAAGACTGGGCGCGGGCGGGAGGGC-3' (reverse)

407 The overhangs containing the restriction endonuclease sites (underlined) and the Kozak sequence
408 (bold) are indicated in lowercase. The purified PCR product was inserted into the multiple cloning
409 site (MCS) of the mEGFP-N1 vector backbone to generate C-terminally tagged TNFR1-EGFP.
410 SacI (QuickCutTM Sac I, Takara Bio, #1627) and SalI (QuickCutTM Sal I, Takara Bio, #1636)
411 restriction endonucleases were used. The digested products were ligated using T4 DNA Ligase
412 (New England Biolabs, #M0202S). The fidelity of the chimeric clone was confirmed through
413 diagnostic restriction digestion and direct sequencing (Eurofins, Bangalore, India).

414 ### Cell culture and transfection

415 HeLa cell line was obtained from the National Center for Cell Science (NCCS) in Pune, India, while
416 THP-1 cell line of American Type Culture Collection (ATCC) origin was generously provided by
417 Dr. Prosenjit Sen from the Indian Association for the Cultivation of Science in Kolkata, India. Both
418 cell lines were cultured in Dulbecco's Modified Eagle Medium (DMEM) (HiMedia, #AL007G)
419 supplemented with 10% fetal bovine serum (FBS) (HiMedia, #RM9955) and 1% penicillin-
420 streptomycin (Antibiotic Solution 100X Liquid, HiMedia, #A001) at 37°C in a humidified
421 incubator with 5% CO2.

422 HeLa cells were transfected with the afore-mentioned plasmids using FuGENE® HD Transfection
423 Reagent (Promega, #E2311), following the manufacturer's protocol. Approximately 1 x 10^5 cells

were seeded in glass-bottom Petri dishes 24 hours before transfection and allowed to reach 70% confluency. Transfection was carried out using 1 μg of plasmid DNA under serum-starved conditions for the first six hours after transfection, and then the cells were incubated with added culture media overnight at 37°C with 5% CO_2. The medium was then replaced with DMEM supplemented with FBS and antibiotics before proceeding with further experiments. For TNFR1-EGFP overexpression-dependent signaling and IRD study, HeLa cells were transfected with 0.1, 0.5, and 1 μg of TNFR1-14aa-EGFP plasmid DNA. Linker length-dependent IRD studies were carried out by transfecting HeLa cells with 1 μg of TNFR1-7aa-EGFP, TNFR1-14aa-EGFP, and TNFR1-21aa-EGFP plasmid DNA. To generate TNFR1 knockdown cells, HeLa cells were transfected with pre-designed siRNA targeting human TNFRSF1A (Sigma-Aldrich/Merck, #SASI_Hs01_00033456, #SASI_Hs01_00033458), along with MISSION® siRNA Universal Negative Control #1 (Sigma-Aldrich/Merck, #SIC001) as the corresponding scrambled control. The transfection was performed using 30, 60, 90, and 120 nM of siRNA and FuGENE® under serum-starved conditions following the standard protocol for the optimization of TNFR1 knockdown efficiency. The transfection mix was incubated at room temperature for 15 minutes before being added drop-wise to the cells. The silenced cells were analyzed 96 hours post-transfection. The optimized 30 nM human TNFRSF1A siRNA was used for the experiments related to knockdown, IRD, and signaling measurements, as described in the result sections. To validate TNFR1-mediated NF-κB nuclear translocation in a 3D gel-like microenvironment, cells were pre-treated with 50 μM zafirlukast (Sigma-Aldrich/Merck, #Z4152) for 16 hours before proceeding with EGFP-p65 transfection.

sTNF-α, drug, and osmolyte treatments

To initiate cytokine stimulation, HeLa cells (1×10^5) were plated in glass-bottomed Petri dishes and incubated overnight at 37°C with 5% CO_2. Subsequently, to deplete secreted cytokines and minimize cellular metabolic activity, the existing DMEM was aspirated, and cells were subjected to serum starvation for 4 hours. Afterward, cells were thoroughly rinsed twice with serum-free DMEM to eliminate any soluble tumor necrosis factor-alpha (sTNF-α) that might be present in the medium. Recombinant human TNF-α protein (ABclonal, #RP00993) was then introduced to the cells at various concentrations (5-100 ng/mL) and for different durations (5-45 minutes), as specified in the results section.

To evaluate the inhibitory effect of Zafirlukast on TNFR1-mediated signaling in HeLa cells, the compound was tested at varying concentrations and incubation times, as described in the Results

456 section. For all subsequent experiments, HeLa cells were subjected to serum starvation for 3 hours,
457 followed by a 1-hour pre-incubation with 100 μM Zafirlukast (Sigma-Aldrich/Merck, #Z4152). To
458 induce osmotic shock in HeLa cells, the standard isotonic DMEM was replaced with hypertonic
459 media (150 mM mannitol (Sigma-Aldrich/Merck, #M9647) dissolved in DMEM) or hypotonic
460 media (75% autoclaved distilled water mixed with 25% DMEM by volume) for the duration
461 specified in the results section. Additionally, to disrupt the actin cytoskeleton, HeLa cells were
462 treated with 2 μM cytochalasin D (CytoD) (Sigma-Aldrich/Merck, #C8273) under serum-starved
463 conditions for 1 hour, unless otherwise stated. Cholesterol depletion in HeLa cells involved a serum
464 starvation for 2 hours, followed by 1 hour incubation with 2 mM methyl-β-cyclodextrin (MβCD)
465 (Sigma-Aldrich/Merck, #C4555). Endocytosis inhibition was performed in TNFR1-EGFP-
466 overexpressing HeLa cells by treating the cells with 80 μM dynasore (Sigma-Aldrich/ Merck,
467 #D7693) for 50 minutes under serum-starved conditions. Prior to dynasore treatment, cells were
468 preincubated in serum-free medium for 1 hour.

469 **Immunofluorescence**

470 HeLa cells were seeded in a glass-bottom plate and incubated overnight in cell culture conditions.
471 They were then fixed with 4% paraformaldehyde (PFA) (HiMedia, #GRM3660) in 1x phosphate-
472 buffered saline (PBS) for 15 minutes. For immunostaining of the plasma membrane-associated
473 TNFR1, the fixed cells were blocked with a 5% BSA solution in 1x PBS for 1 hour at room
474 temperature, without permeabilizing the plasma membrane. After three washes with 1x PBS, the
475 cells were incubated with a 1:500 dilution of TNFR1/TNFRSF1A rabbit pAb (Invitrogen, # PA5-
476 95585), in antibody dilution buffer (3% BSA in 1x PBS) overnight at 4°C. Subsequently, the cells
477 were washed thrice with 1x PBS and incubated with Alexa Fluor-594 conjugated secondary
478 antibody (1:200 dilution, Anti-rabbit IgG, Cell Signaling Technology, #8889) for 1 hour at room
479 temperature. After three washes with 1x PBS, the cells were ready for imaging. To validate our
480 TNFR1-EGFP chimeric construct, 18-20 hours post-transfected, HeLa TNFR1-EGFP cells were
481 fixed and prepared for membrane-associated TNFR1 immunostaining following the protocol
482 described above. This approach allowed us to visualize most plasma-membrane-associated TNFR1-
483 EGFP expressions (**Fig. S1B**) of the TNFR1-EGFP chimeric construct within the cells.

484 For immunostaining of NF-κB (p65) after fixation of the HeLa cells with 4% PFA in 1x PBS for
485 15 mins, they were permeabilized with 0.1% Triton X-100 (Sisco Research Laboratories, #64518)
486 in 1x PBS for 4-5 mins. Then the fixed cells were blocked with a 5% BSA solution in 1x PBS for
487 1 hour at room temperature. After three washes with 1x PBS, the cells were incubated with a 1:500

488 dilution of NF-κB p65 mouse mAb (Cell Signaling Technology, #6956) in antibody dilution buffer
489 (3% BSA in 1x PBS) overnight at 4°C. Subsequently, the cells were washed thrice with 1x PBS
490 and incubated with Alexa Fluor-594 conjugated secondary antibody (1:200 dilution, Anti-mouse
491 IgG, Cell Signaling Technology, #8890) for 1 hour at room temperature. After three washes with
492 1x PBS, the cells were ready for imaging. The nuclei were counterstained with Hoechst 33342
493 (ThermoFisher, #62249) (0.5 µg/mL, 5 minutes).

494 **Generation of TNFR1–EGFP Constructs with Altered Linker Lengths**

495 To examine the effect of linker flexibility on TNFR1 organization and signaling, TNFR1–EGFP
496 fusion constructs were generated containing short (7 amino acids) and long (21 amino acids)
497 linkers, derived from the parental construct with a 14–amino acid flexible linker (TNFR1-14aa-
498 EGFP). The cloning was performed by Gibson assembly (GeneArt™ Gibson Assembly® HiFi
499 Cloning Kit, Invitrogen, # A46627) using primers designed to modify the linker region between
500 TNFR1 and mEGFP.

501 For the short-linker construct (TNFR1-7aa-EGFP), the entire plasmid was PCR-amplified using
502 Phusion™ High–Fidelity DNA Polymerase (ThermoFisher, # F530S) with primers that deleted 21
503 base pairs from the original linker sequence, thereby halving its length while maintaining the
504 reading frame. Primer sequences were as follows (lowercase letters denote Gibson overhangs):

Primer	**Sequence (5′–3′)**
7 aa Forward	gtaccgGCCACCATGGTGAGCAAGGGC
7 aa Reverse	ggtggcCGGTACCGTCGACTCTCTGAGAAG

505 Following Gibson assembly, recombinant plasmids were electroporated into *E. coli* strain MC1061.
506 Colonies were screened by BamHI digestion (QuickCut™ BamHI, Takara Bio, #1605), as the
507 shortened linker design eliminated a BamHI site, enabling rapid verification.

508 For the long-linker construct (TNFR1-21aa-EGFP), PCR amplification was performed with primers
509 that inserted 21 additional base pairs encoding a glycine–serine (GS)-rich motif (GGSGSSG) into
510 the linker region, extending it to 21 amino acids. This flexible GS sequence was selected to preserve
511 structural integrity and prevent steric interference (*71*). Primer sequences were:

Primer	Sequence (5′–3′)
21 aa Forward	atccggctcatcggggGAGTCGACGGTACCGCG
21 aa Reverse	gatgagccggatccgcCTCTGAGAAGACTGGGCGC

512 Following Gibson assembly, plasmids were electroporated into *E. coli* MC1061, and transformants
513 were screened by PCR using a promoter-specific forward primer and a reverse primer annealing to
514 the newly inserted linker sequence. Amplification was observed only from the modified construct
515 and not from the parental TNFR1–EGFP plasmid, confirming the successful generation of the
516 TNFR1–21aa–EGFP plasmid. Verification primers were:

Primer	Sequence (5′–3′)
21 aa Promoter Forward	GGCCCGCCTGGCTGACCG
21 aa Linker Reverse	CCCGATGAGCCGGATCCGCC

517 All constructs were validated by Sanger sequencing (Eurofins, Bangalore, India) to confirm the
518 fidelity of the linker modifications.

519 **Cell extracts and immunoblotting**

520 HeLa cells (1 x 10^5) were cultured in 35 mm dishes and incubated overnight at 37°C with 5% CO2
521 until reaching approximately 70% confluency. Following this, the cells were either transfected with
522 siRNA or treated with various drugs for specified durations before proceeding with cell lysate
523 preparation. The cells were rinsed with ice-cold PBS and then lysed using 100 µL of RIPA buffer
524 (50 mM Tris HCl, 150 mM NaCl, 1.0% (v/v) NP-40, 0.5% (w/v) sodium deoxycholate, 1.0 mM
525 EDTA, 0.1% (w/v) SDS, and 0.01% (w/v) sodium azide, pH 7.4), supplemented with Protease and
526 Phosphatase Inhibitor Cocktail (Sigma-Aldrich/Merck, #PPC1010). The lysates were incubated on
527 ice for 15 minutes, and then the contents of each dish were transferred to the respective 1.5 mL
528 microcentrifuge tubes. Total cell extracts were obtained by agitating the lysates at 4°C for 30
529 minutes. The cell lysates were centrifuged at 12,000 g for 20 minutes at 4°C, and the supernatants
530 were collected in fresh tubes kept on ice.

531 The protein concentration was determined using the Bradford assay, and subsequently, 40-50 µg of
532 total protein per condition was loaded onto a 12% polyacrylamide gel after boiling the samples in

533 2X Laemmli sample buffer (4% (w/v) SDS, 20% (v/v) glycerol, 120 mM Tris-HCl pH 6.8, 0.02%
534 bromophenol blue) containing 5% β-mercaptoethanol for 15 minutes. The samples were then
535 immediately resolved on SDS-polyacrylamide gel electrophoresis (PAGE), and the proteins were
536 transferred to Immobilon®-P PVDF membrane (Merck Millipore, #IPVH00010). Immunoblots
537 were blocked with 5% bovine serum albumin (BSA) in tris-buffered saline (TBS) containing 0.1%
538 Tween-20 (TBS-T) for 1 hour at room temperature. The membrane was then probed with specific
539 primary antibodies diluted 1:1000 in antibody dilution buffer (3% BSA in TBS-T) and incubated
540 overnight at 4°C - either anti-TNFR1 rabbit monoclonal antibody (Invitrogen, #MA5-14899) or
541 anti-β-Actin mouse monoclonal antibody (Santa Cruz Biotechnology, #sc-47778). Following
542 primary antibody incubation, the membranes were washed thrice with TBS-T for 5 minutes each
543 and then incubated with the respective secondary antibodies at room temperature for 1 hour - either
544 1:10,000 horseradish peroxidase (HRP)-conjugated goat anti-rabbit IgG (Sigma-Aldrich/Merck,
545 #A9169) or anti-mouse IgG (Sigma-Aldrich/Merck, #A9044). A standard Pre-stained Protein
546 Ladder (HiMedia, #MBT092) was used to determine the molecular weight of the proteins of
547 interest.

548 For the detection of GFP, the same procedure was followed, with the exception that the primary
549 antibody used was a monoclonal anti-GFP antibody (Santa Cruz Biotechnology, #sc-9996) at a
550 dilution of 1:1000. For immunoblotting of p65 and phospho-p65, the primary antibodies used were
551 NF-κB p65 (L8F6) Mouse monoclonal antibody (Cell Signaling Technology, #6956) and Phospho-
552 NF-κB p65 (Ser536) (93H1) Rabbit monoclonal antibody (Cell Signaling Technology, #3033),
553 each at a 1:1000 dilution. The corresponding HRP-conjugated secondary antibodies were the same
554 as described before.

555 Immunodetection was performed using standard chemiluminescence procedures, and densitometric
556 analysis was carried out using ImageJ software.

557 **Immunoprecipitation**

558 HeLa cells (~8×10^6) were seeded in 10-cm culture dishes and incubated overnight. Cells were
559 lysed on ice in buffer containing 50 mM Tris-HCl (pH 7.4), 150 mM NaCl, 1% NP-40, 0.1% SDS,
560 and 0.5% sodium deoxycholate, supplemented with protease and phosphatase inhibitor cocktail
561 (Sigma, #PPC1010). Lysates were incubated on ice for 15 min and centrifuged at 15,000 × *g* for 20
562 min at 4°C to remove debris. Protein concentrations were determined using the Bradford assay.

563 To minimize nonspecific binding, lysates were precleared with 50 µL of protein A/G–PLUS
564 agarose beads (Santa Cruz, #sc-2003) for 1 hour at 4°C. For immunoprecipitation, 3 mg of
565 precleared lysate was incubated overnight at 4°C with 10 µL of anti-TNFR1/TNFRSF1A rabbit
566 polyclonal antibody (ABclonal, #A1540) and 50 µL of protein A/G–PLUS agarose beads. Immune
567 complexes were recovered by centrifugation and washed three times with lysis buffer before
568 separation by SDS–PAGE on 10% Tris-glycine gels.

569 Proteins were transferred to PVDF membranes (Millipore) and blocked in TBS containing 0.1%
570 Tween-20 and 5% BSA for 1 hour at room temperature. Membranes were probed overnight at 4°C
571 with rabbit anti–TNF-α antibody (Thermo Fisher, #PA5-19810) or anti–TNFR1/TNFRSF1A
572 antibody (ABclonal, #A1540), each at a 1:1000 dilution. GAPDH served as a loading control and
573 was detected using a mouse monoclonal anti-GAPDH antibody (ABclonal, #AC033). After
574 washing, membranes were incubated with horseradish peroxidase–conjugated secondary antibodies
575 for 1 hour at room temperature: goat anti-rabbit IgG (1:10,000; Sigma-Aldrich, #A0545) and goat
576 anti-mouse IgG (1:10,000; Sigma-Aldrich/Merck, #A9044). Detection was performed using
577 enhanced chemiluminescence.

578 **Flow cytometry**

579 Before the flow cytometry assay, HeLa cells (1 x 10^5) were cultured in 35 mm Petri dishes overnight
580 for 16 hours under standard cell culture conditions. Following this, the cells were exposed to various
581 treatments as described in the results section. Following treatment, cells were washed with ice-cold
582 1× PBS, detached, pelleted in microfuge tubes, and fixed with 4% PFA for 15 minutes on ice. The
583 cells were then washed three times with ice-cold 1× PBS and blocked with 5% BSA in 1× PBS for
584 20 minutes. Subsequently, they were incubated for 1 hour with TNFR1/TNFRSF1A rabbit pAb
585 (Invitrogen, #PA5-95585; 1:500) prepared in FACS buffer (3% BSA in 1× PBS, 2 mM EDTA).
586 After two washes with ice-cold FACS buffer, cells were incubated with Alexa Fluor 488 conjugated
587 anti-rabbit IgG secondary antibody (Cell Signaling Technology, #4412; 1:200) for 30 minutes,
588 followed by three additional washes with ice-cold FACS buffer. Subsequently, the cells were
589 suspended in FACS buffer to prepare them for flow cytometric analysis. A total of 10^4 cells were
590 recorded for each condition in the FITC channel to measure the cell surface expression of TNFR1
591 relative to unstained and control conditions. Data acquisition was performed using a BD FACS
592 Aria III, and the respective fluorescence count histogram and normalized mean fluorescence
593 intensities (MFI) were analyzed using Flowing Software and then plotted using Origin 2019b. The
594 signaling efficacy of TNFR1 was quantified by determining the mean p65 N/C ratio per plasma

595 membrane-associated TNFR1 molecule, calculated using the MFI obtained from flow cytometry in
596 each condition (with or without sTNF-α).

597 **TNFR1-EGFP chimeric construct validation and cluster area analysis using confocal**
598 **microscopy**

599 To validate the TNFR1-EGFP chimeric construct, TNFR1 was immunostained in TNFR1-EGFP
600 overexpressing cells without plasma membrane permeabilization as previously stated. The cells
601 were imaged using a Zeiss LSM 780 light scanning confocal system with a 63x oil immersion
602 objective, using two channels for green (TNFR1-EGFP) and red (Alexa Fluor-594, endogenous)
603 fluorescence. Merging the two channels resulted in yellow color in the TNFR1-EGFP cluster
604 regions, indicating colocalization, and confirming that the anti-TNFR1 pAb recognizes our TNFR1-
605 EGFP construct.

606 For TNFR1 endogenous and exogenous cluster area measurements in different experiments, as
607 stated in the result sections, images were captured using a Zeiss LSM 780 light scanning confocal
608 system with a 63x oil immersion objective in airy scan mode. Then, both endogenous and
609 exogenous (TNFR1-EGFP) clusters were segregated using intensity-based thresholding in ImageJ,
610 and the area of the clusters was measured using the segregated ROI in measurement plugins.

611 **Quantification of TNFR1-EGFP clusters on the plasma membrane over time**

612 HeLa cells overexpressing TNFR1-EGFP were stained with 0.5x CellMask Orange (CellMask™
613 Plasma Membrane Stains, Invitrogen, #C10045) at 4-, 12-, 18-, and 24-hours post-transfection. The
614 live HeLa cells overexpressing TNFR1-EGFP and stained with CellMask Orange were imaged
615 using a Zeiss LSM 780 light scanning confocal system. The imaging was performed with a 63x oil
616 immersion objective in airy scan super-resolution mode, with a 0.4μm Z-step size, using two
617 appropriate channels for green (EGFP) and orange (CellMask Orange) fluorescence. Image analysis
618 was performed in ImageJ, where the cell boundary was determined from the CellMask Orange
619 image using intensity-based thresholding. Clusters of TNFR1-EGFP that overlapped with the
620 CellMask Orange-derived cell boundary were classified as plasma membrane-associated clusters.
621 Total and plasma membrane-associated TNFR1-EGFP cluster counting of a cell was conducted
622 using the 3D object counter plugin in ImageJ. The percentage of fractional plasma membrane-
623 associated clusters was then calculated at different time points.

624 **Nuclear-to-cytoplasmic (N/C) p65 measurement**

625 Fluorescence images of p65-immunostained HeLa cells were captured using a Zeiss AxioObserver
626 Z1 microscope with a 40x air objective to measure the nuclear-to-cytoplasmic ratio (N/C). Z-stacks
627 of randomly selected cell populations were obtained for analysis. Image analysis using ImageJ was
628 performed to determine the N/C ratio of p65. The nuclear portion of p65 was quantified by selecting
629 a region of interest (ROI) in the focused Z-plane of the nucleus, as identified from Hoechst staining
630 images. The mean fluorescence intensity of nuclear p65 (N) was measured using this ROI from the
631 p65 immunostaining z-stack image. For cytoplasmic p65 (C), the total fluorescence intensity of the
632 cytoplasm was measured in areas where the cytoplasm was in focus. The total nuclear fluorescence
633 intensity was then subtracted from this value. The mean cytoplasmic p65 intensity was calculated
634 by dividing the total cytoplasmic intensity by the cytoplasmic area, which was determined by
635 subtracting the nuclear area from the total protoplasmic area.

636 **Cell culture in a 3D gel-like microenvironment**

637 HeLa cells (1 x 10^5) were seeded in a glass-bottom Petri dish and allowed to adhere overnight under
638 standard cell culture conditions. Subsequently, the medium was aspirated, and a solution of 1%
639 low-melting HiRes Agarose (Genetix, Puregene, #PG-432) in DMEM was carefully added to cover
640 the adherent cells, forming a thin gel layer. The Petri dish was then briefly incubated at 4°C for 2
641 minutes to facilitate rapid gel formation. Fresh media was gently added on top of the agarose gel
642 cover to prevent dehydration. The cells were maintained within this 3D gel-like microenvironment
643 for the durations specified in the results section.

644 **ROS measurements**

645 HeLa cells were seeded in a 96-well plate at equal density (1 x 10^4 cells) and allowed to grow for
646 24 hours. Subsequently, the cells were treated with 2 μM cytochalasin D (CytoD) (Sigma-
647 Aldrich/Merck, #C8273) for 1 hour, with or without pre-treatment with 500 μM L-Ascorbic acid
648 (Vitamin C) (Sigma-Aldrich/Merck, #A4544) for 1 hour. For reactive oxygen species (ROS)
649 analysis, cells were stained with 10 μM H_2DCFDA (Sigma-Aldrich/Merck, #287810) for 30
650 minutes following each treatment and then lysed with 95% dimethyl sulphoxide (DMSO)
651 (HiMedia, #MB058). The fluorescence intensity of each cell sample was measured using a
652 spectrofluorometer (SpectraMax iD5 Multi-Mode Microplate Reader, Molecular Devices) with
653 excitation/emission wavelengths set at 485 nm/535 nm.

654 **Fluorescence Anisotropy Imaging Microscopy (FAIM)**

655 Fluorescence anisotropy of TNFR1-EGFP was measured in HeLa cells overexpressing the protein,
656 18-20 hours post-transfection. The fluorescence anisotropy was determined using a well-
657 established principle (*36*). Imaging was performed with a Zeiss AxioObserver Z1 epifluorescence
658 microscope equipped with a 63x oil immersion objective (NA 1.4) and a mercury arc lamp (HXP
659 120 V) as the light source. Horizontally polarized excitation light was achieved by passing the light
660 through a linear polarizer (ThorLabs) in the excitation path. In the emission path, a polarizing beam
661 splitter (DV2, Photometrics) was utilized to divide the resulting polarized fluorescence signal into
662 parallel and perpendicular polarizations. The fluorescence from these two polarizations was
663 simultaneously captured by a CMOS camera (Hamamatsu Orca Flash 4.0 C13440), with one half
664 of the image representing the parallel channel ($I_{\parallel}$) and the other half representing the perpendicular
665 channel ($I_{\perp}$). Due to deformations in the optical path and thermal fluctuations, there was partial
666 overlap between the two halves ($I_{\parallel}$, $I_{\perp}$). To correct this, image registration of each cluster of
667 TNFR1-EGFP in the two channels was performed by intensity cross-correlation using the particle
668 image velocimetry (PIV) method, followed by MATLAB's mono-modal intensity-based
669 registration tool (**fig. S9C**). Subsequently, the fluorescence anisotropy (r) in each pixel of the
670 clusters was calculated using the equation:

671 $$r = \frac{I_{\parallel} - g\, I_{\perp}}{I_{\parallel} + 2\, g\, I_{\perp}}$$

672 Where g is the instrumental correction factor (G-factor, ${}^{I_{\parallel}}/_{I_{\perp}}$), determined by measuring 100 nM
673 fluorescein in water in each pixel. A custom MATLAB code was developed for TNFR1-EGFP
674 cluster image registration and anisotropy calculation. Verification of homo-FRET was carried out
675 through sequential photobleaching at 100% lamp power for 20 seconds, with imaging of the same
676 cell before and after photobleaching. Background correction was performed by subtracting the
677 mean fluorescence intensity of regions without transfected cells in the imaging field. The
678 fluorescence anisotropy of HeLa-mEGFP and HeLa-2GFP cells was assessed using in-house
679 ImageJ code. To achieve image registration, fluorescent polystyrene microspheres with a 200 nm
680 diameter were dried onto a glass coverslip and imaged in the same configuration as the anisotropy
681 measurements. The Descriptor-based Registration plugin of Fiji (ImageJ) was employed for this
682 purpose.

683 From the anisotropy calculation of TNFR1-EGFP clusters, we obtained a total intensity map ($I_{\parallel} +$
684 $2\, g\, I_{\perp}$) and a fluorescence anisotropy map (r) for each cluster. To simplify our analysis, we divided
685 the fluorescence anisotropy map of each TNFR1-EGFP cluster into two regions, which we named

686 core (central region) and rim (peripheral region), based on the intensity map. In the intensity map,
687 the region with intensity greater than or equal to 70% of the maximum intensity of the cluster was
688 designated as the core, while the region with intensity greater than 10% of the maximum intensity
689 was considered the whole cluster. The rim region was then obtained by subtracting the core region
690 from the whole cluster. Therefore, the rim region comprised the intensity values between >10% and
691 <70% of the maximum intensity of the cluster (**Fig. 1, D and E**). A custom ImageJ code was
692 developed to perform this segmentation. Using the same region of interest (ROI) from the intensity
693 map, we extract the core and rim anisotropy values from the anisotropy map.

694 **Fluorescence Lifetime Imaging Microscopy (FLIM)**

695 Flipper-TR (Spirochrome, #SC020) was used to assess the plasma membrane tension of cells
696 through fluorescence lifetime imaging. Fluorescence lifetime measurements of Flipper-TR were
697 conducted using an Olympus IX71 microscope with a 60x water immersion objective (NA 1.2)
698 fitted with a time-correlated single-photon counting (TCSPC) module from PicoQuant, and excited
699 with a picosecond 470 nm laser (PicoQuant). The fluorescence lifetime data for each pixel were
700 analyzed by fitting them to a bi-exponential decay curve using SymPhoTime64 software. To
701 quantify the lifetime, the higher amplitude lifetime (τ_1) at each pixel was used, as detailed in the
702 referenced article (*53*). For each cell, τ_1 values were averaged over the region of interest (ROI)
703 corresponding to the plasma membrane. To assess the effect of a 3D gel-like microenvironment on
704 membrane tension, HeLa cells were incubated under a layer of low-melting agarose overnight,
705 while THP-1 cells were incubated for 4 hours. Corresponding 2D control cells were seeded at the
706 same time, 12 hours before agarose overlay. Both 2D (control) and 3D (agarose-covered) cells were
707 simultaneously incubated with 200 nM Flipper-TR for 15–20 minutes before performing all
708 fluorescence lifetime measurements.

709 **Fluorescence Recovery after Photobleaching (FRAP)**

710 FRAP experiments were conducted on HeLa cells overexpressing TNFR1-EGFP using a Zeiss
711 LSM 780 light scanning confocal system with a 63x oil immersion objective. TNFR1-EGFP
712 clusters were first imaged with 2% laser power and then bleached using 60% laser power at 488
713 nm, followed by the acquisition of time-lapse imaging for 90 seconds with 1-second intervals using
714 2% laser power of the same region. The percentage of recovery after bleaching was calculated
715 relative to the pre-bleached condition by comparing the mean fluorescence intensity of the clusters

716 over time to the pre-bleach mean fluorescence intensity. This value was then plotted against time
717 to visualize the recovery process.

718 **IRM**

719 Cell imaging was conducted on a Nikon Eclipse Ti-E motorized inverted microscope (Nikon,
720 Japan), featuring adjustable field and aperture diaphragms, a 60X Plan Apo lens (NA 1.22, water
721 immersion), and a 1.5X external magnification. The microscope was positioned on an onstage 37°C
722 incubator (Tokai Hit, Japan). Imaging was facilitated using an s-CMOS camera (ORCA Flash 4.0,
723 Hamamatsu, Japan). Illumination was provided by a 100W mercury arc lamp, employing an
724 interference filter (546±12 nm) and a 50-50 beam splitter. For Interference Reflection Microscopy
725 (IRM), movies comprised 2048 frames (20 frames/s), recorded with an exposure time of 50 ms.
726 Analysis of IRM images to obtain fluctuation tension was performed (*72*) using three different
727 steps. At first, the calibration factor is obtained to convert intensity to relative height, and pixels
728 corresponding to the first branch region (FBR) of the interference pattern are identified.
729 Subsequently, the time series of height was obtained for each pixel, and the amplitude of
730 fluctuations (SD_{time} and SD_{space}) was obtained for FBRs. Finally, for every FBR, the power spectral
731 density (PSD) was obtained and fitted to an adapted Helfrich-Calham model to extract the
732 fluctuation tension and other parameters (*73*).

733 **TIRF imaging**

734 TIRF Microscopy utilized an inverted microscope (Olympus IX-83, Olympus, Japan) equipped
735 with a 100X 1.49 NA oil immersion TIRF objective (PlanApo, Olympus). The imaging setup
736 included an s-CMOS camera (ORCA Flash 4.0, Hamamatsu, Japan) and a 488 nm laser source.
737 Image acquisition was performed with an exposure time of 200 ms, achieving a penetration depth
738 of approximately 70 nm. For cluster size analysis from TIRF images in different conditions, as
739 depicted in the result sections, local thresholding was performed to detect objects using MATLAB.
740 All immobile clusters were manually identified, and the area of the objects from the region
741 properties was used for comparison.

742 Time-lapse imaging was performed in TIRF mode on TNFR1-EGFP–overexpressing HeLa cells
743 (**fig. S1C**) using continuous acquisition with a 50-ms exposure for 5 minutes, without intervals, to
744 assess receptor cluster stoichiometry.

745 **Statistical analysis**

Individual measurements from technical replicates within each treatment group were pooled to generate a unified dataset of biological replicates. Variations in mean values of measurements taken from the same cells before and after treatment were assessed using a paired two-tailed Student's *t*-test. For comparisons between two distinct cell populations, an unpaired two-tailed Student's *t*-test was applied, assuming that sufficiently large sample sizes approximate a normal distribution. When comparisons involved more than two groups, a one-way ANOVA was performed. Details of the statistical tests applied are provided in the respective figure legends. All statistical analyses and graphical representations were performed using Origin 2019b.

References

H. T. Idriss, J. H. Naismith, TNF? and the TNF receptor superfamily: Structure-function relationship(s). *Microsc Res Tech* **50**, 184–195 (2000).

É. S. Vanamee, D. L. Faustman, Structural principles of tumor necrosis factor superfamily signaling. *Sci Signal* **11** (2018).

M. Croft, W. Duan, H. Choi, S.-Y. Eun, S. Madireddi, A. Mehta, TNF superfamily in inflammatory disease: translating basic insights. *Trends Immunol* **33**, 144–152 (2012).

G. van Loo, M. J. M. Bertrand, Death by TNF: a road to inflammation. *Nat Rev Immunol* **23**, 289–303 (2023).

Y. Takei, R. Laskey, Tumor Necrosis Factor α Regulates Responses to Nerve Growth Factor, Promoting Neural Cell Survival but Suppressing Differentiation of Neuroblastoma Cells. *Mol Biol Cell* **19**, 855–864 (2008).

A. Bhardwaj, B. B. Aggarwal, Receptor-mediated choreography of life and death. *J Clin Immunol* **23**, 317–32 (2003).

O. Micheau, J. Tschopp, Induction of TNF Receptor I-Mediated Apoptosis via Two Sequential Signaling Complexes. *Cell* **114**, 181–190 (2003).

S. Yang, C. Xie, Y. Chen, J. Wang, X. Chen, Z. Lu, R. R. June, S. G. Zheng, Differential roles of TNFα-TNFR1 and TNFα-TNFR2 in the differentiation and function of CD4+Foxp3+ induced Treg cells in vitro and in vivo periphery in autoimmune diseases. *Cell Death Dis* **10**, 27 (2019).

J. D. Webster, D. Vucic, The Balance of TNF Mediated Pathways Regulates Inflammatory Cell Death Signaling in Healthy and Diseased Tissues. *Front Cell Dev Biol* **8** (2020).

G. Chen, D. V. Goeddel, TNF-R1 Signaling: A Beautiful Pathway. *Science (1979)* **296**, 1634–1635 (2002).

R. A. Smith, C. Baglioni, The active form of tumor necrosis factor is a trimer. *Journal of Biological Chemistry* **262**, 6951–6954 (1987).

J. H. Naismith, B. J. Brandhuber, T. Q. Devine, S. R. Sprang, Seeing double: Crystal structures of the type I TNF receptor. *Journal of Molecular Recognition* **9**, 113–117 (1996).

D. W. Banner, A. D'Arcy, W. Janes, R. Gentz, H.-J. Schoenfeld, C. Broger, H. Loetscher, W. Lesslauer, Crystal structure of the soluble human 55 kd TNF receptor-human TNFβ complex: Implications for TNF receptor activation. *Cell* **73**, 431–445 (1993).

C. Karathanasis, J. Medler, F. Fricke, S. Smith, S. Malkusch, D. Widera, S. Fulda, H. Wajant, S. J. L. van Wijk, I. Dikic, M. Heilemann, Single-molecule imaging reveals the oligomeric state of functional TNFα-induced plasma membrane TNFR1 clusters in cells. *Sci Signal* **13**, 5647 (2020).

K. Kucka, H. Wajant, Receptor Oligomerization and Its Relevance for Signaling by Receptors of the Tumor Necrosis Factor Receptor Superfamily. *Front Cell Dev Biol* **8** (2021).

F. Fricke, S. Malkusch, G. Wangorsch, J. F. Greiner, B. Kaltschmidt, C. Kaltschmidt, D. Widera, T. Dandekar, M. Heilemann, Quantitative single-molecule localization microscopy combined with rule-based modeling reveals ligand-induced TNF-R1 reorganization toward higher-order oligomers. *Histochem Cell Biol* **142**, 91–101 (2014).

F. K.-M. Chan, H. J. Chun, L. Zheng, R. M. Siegel, K. L. Bui, M. J. Lenardo, A Domain in TNF Receptors That Mediates Ligand-Independent Receptor Assembly and Signaling. *Science (1979)* **288**, 2351–2354 (2000).

É. S. Vanamee, D. L. Faustman, The benefits of clustering in TNF receptor superfamily signaling. *Front Immunol* **14** (2023).

C. S. Lim, J. Lee, J. W. Kim, J.-O. Lee, Highly ordered clustering of TNFα and BAFF ligand-receptor-intracellular adaptor complexes on a lipid membrane. *Nat Commun* **16**, 5551 (2025).

M. Branschädel, A. Aird, A. Zappe, C. Tietz, A. Krippner-Heidenreich, P. Scheurich, Dual function of cysteine rich domain (CRD) 1 of TNF receptor type 1: Conformational stabilization of CRD2 and control of receptor responsiveness. *Cell Signal* **22**, 404–414 (2010).

L. Zhao, Q. Fu, L. Pan, A. Piai, J. J. Chou, The Diversity and Similarity of Transmembrane Trimerization of TNF Receptors. *Front Cell Dev Biol* **8** (2020).

P. E. Morton, C. Perrin, J. Levitt, D. R. Matthews, R. J. Marsh, R. Pike, D. Mcmillan, A. Maloney, S. Poland, S. Ameer-Beg, M. Parsons, "TNFR1 membrane reorganization promotes distinct modes of TNFα signaling" (2019); http://stke.sciencemag.org/.

M. P. Boldin, I. L. Mett, E. E. Varfolomeev, I. Chumakov, Y. Shemer-Avni, J. H. Camonis, D. Wallach, Self-association of the "Death Domains" of the p55 Tumor Necrosis Factor (TNF) Receptor and Fas/APO1 Prompts Signaling for TNF and Fas/APO1 Effects. *Journal of Biological Chemistry* **270**, 387–391 (1995).

A. Caminero, M. Comabella, X. Montalban, Tumor necrosis factor alpha (TNF-α), anti-TNF-α and demyelination revisited: An ongoing story. *J Neuroimmunol* **234**, 1–6 (2011).

A. Caminero, M. Comabella, X. Montalban, Role of tumour necrosis factor (TNF)-α and *TNFRSF1A* R92Q mutation in the pathogenesis of TNF receptor-associated periodic syndrome and multiple sclerosis. *Clin Exp Immunol* **166**, 338–345 (2011).

F. C. Kimberley, A. A. Lobito, R. M. Siegel, G. R. Screaton, Falling into TRAPS – receptor misfolding in the TNF receptor 1-associated periodic fever syndrome. *Arthritis Res Ther* **9**, 217 (2007).

G.-M. Deng, L. Zheng, F. K.-M. Chan, M. Lenardo, Amelioration of inflammatory arthritis by targeting the pre-ligand assembly domain of tumor necrosis factor receptors. *Nat Med* **11**, 1066–72 (2005).

F. Hadziselimovic, L. R. Emmons, H. Gallati, Soluble tumour necrosis factor receptors p55 and p75 in the urine monitor disease activity and the efficacy of treatment of inflammatory bowel disease. *Gut* **37**, 260–3 (1995).

A. A. Lobito, F. C. Kimberley, J. R. Muppidi, H. Komarow, A. J. Jackson, K. M. Hull, D. L. Kastner, G. R. Screaton, R. M. Siegel, Abnormal disulfide-linked oligomerization results in ER retention and altered signaling by TNFR1 mutants in TNFR1-associated periodic fever syndrome (TRAPS). *Blood* **108**, 1320–1327 (2006).

Y.-F. Chen, P. Jobanputra, P. Barton, S. Jowett, S. Bryan, W. Clark, A. Fry-Smith, A. Burls, A systematic review of the effectiveness of adalimumab, etanercept and infliximab for the treatment of rheumatoid arthritis in adults and an economic evaluation of their cost-effectiveness. *Health Technol Assess (Rockv)* **10** (2006).

H. Wajant, Principles of antibody-mediated TNF receptor activation. *Cell Death Differ* **22**, 1727–41 (2015).

X. Yu, S. James, J. H. Felce, B. Kellermayer, D. A. Johnston, H. T. C. Chan, C. A. Penfold, J. Kim, T. Inzhelevskaya, C. I. Mockridge, Y. Watanabe, M. Crispin, R. R. French, P. J. Duriez, L. R. Douglas, M. J. Glennie, M. S. Cragg, TNF receptor agonists induce distinct receptor clusters to mediate differential agonistic activity. *Commun Biol* **4**, 772 (2021).

N. Weinelt, C. Karathanasis, S. Smith, J. Medler, S. Malkusch, S. Fulda, H. Wajant, M. Heilemann, S. J. L. van Wijk, Quantitative single-molecule imaging of TNFR1 reveals zafirlukast as antagonist of TNFR1 clustering and TNFα-induced NF-κB signaling. *J Leukoc Biol* **109**, 363–371 (2021).

C. H. Lo, N. Vunnam, A. K. Lewis, T.-L. Chiu, B. E. Brummel, T. M. Schaaf, B. D. Grant, P. Bawaskar, D. D. Thomas, J. N. Sachs, An Innovative High-Throughput Screening Approach for Discovery of Small Molecules That Inhibit TNF Receptors. *SLAS Discov* **22**, 950–961 (2017).

S. Ghosh, S. Saha, D. Goswami, S. Bilgrami, S. Mayor, "Dynamic Imaging of Homo-FRET in Live Cells by Fluorescence Anisotropy Microscopy" (2012), pp. 291–327.

J. R. Lakowicz, Principles of fluorescence spectroscopy. *Principles of Fluorescence Spectroscopy*, 1–954 (2006).

S. Ganguly, A. H. A. Clayton, A. Chattopadhyay, Organization of higher-order oligomers of the serotonin$_{1}$(A) receptor explored utilizing homo-FRET in live cells. *Biophys J* **100**, 361–8 (2011).

P. Sharma, R. Varma, R. C. Sarasij, Ira, K. Gousset, G. Krishnamoorthy, M. Rao, S. Mayor, Nanoscale Organization of Multiple GPI-Anchored Proteins in Living Cell Membranes. *Cell* **116**, 577–589 (2004).

Z. J. Chen, L. J. Sun, Nonproteolytic Functions of Ubiquitin in Cell Signaling. *Mol Cell* **33**, 275–286 (2009).

I. E. Wertz, V. M. Dixit, Regulation of death receptor signaling by the ubiquitin system. *Cell Death Differ* **17**, 14–24 (2010).

A. T. Ting, M. J. M. Bertrand, More to Life than NF-κB in TNFR1 Signaling. *Trends Immunol* **37**, 535–545 (2016).

T. Ha, T. Enderle, D. F. Ogletree, D. S. Chemla, P. R. Selvin, S. Weiss, Probing the interaction between two single molecules: fluorescence resonance energy transfer between a single donor and a single acceptor. *Proceedings of the National Academy of Sciences* **93**, 6264–6268 (1996).

J. Hummert, K. Yserentant, T. Fink, J. Euchner, Y. X. Ho, S. A. Tashev, D.-P. Herten, Photobleaching step analysis for robust determination of protein complex stoichiometries. *Mol Biol Cell* **32** (2021).

M. S. Dietz, D. Haße, D. M. Ferraris, A. Göhler, H. H. Niemann, M. Heilemann, Single-molecule photobleaching reveals increased MET receptor dimerization upon ligand binding in intact cells. *BMC Biophys* **6**, 6 (2013).

E. Macia, M. Ehrlich, R. Massol, E. Boucrot, C. Brunner, T. Kirchhausen, Dynasore, a Cell-Permeable Inhibitor of Dynamin. *Dev Cell* **10**, 839–850 (2006).

P. Biswas, P. Roy, S. Jana, D. Ray, J. Das, B. Chaudhuri, R. R. Basunia, B. Sinha, D. K. Sinha, Exploring the role of macromolecular crowding and TNFR1 in cell volume control. *Elife* **13** (2024).

N. Vunnam, M. Yang, C. H. Lo, C. Paulson, W. D. Fiers, E. Huber, M. Been, D. M. Ferguson, J. N. Sachs, Zafirlukast Is a Promising Scaffold for Selectively Inhibiting TNFR1 Signaling. *ACS bio & med chem Au* **3**, 270–282 (2023).

H. Wajant, P. Scheurich, TNFR1-induced activation of the classical NF-κB pathway. *FEBS J* **278**, 862–876 (2011).

J. S. Kelloway, Zafirlukast: The First Leukotreene-Receptor Antagonist Approved for the Treatment of Asthma. *Annals of Pharmacotherapy* **31**, 1012–1021 (1997).

E. Sitarska, A. Diz-Muñoz, Pay attention to membrane tension: Mechanobiology of the cell surface. *Curr Opin Cell Biol* **66**, 11–18 (2020).

M. Simunovic, E. Evergren, I. Golushko, C. Prévost, H.-F. Renard, L. Johannes, H. T. McMahon, V. Lorman, G. A. Voth, P. Bassereau, How curvature-generating proteins build scaffolds on membrane nanotubes. *Proceedings of the National Academy of Sciences* **113**, 11226–11231 (2016).

M. Simunovic, G. A. Voth, Membrane tension controls the assembly of curvature-generating proteins. *Nat Commun* **6**, 7219 (2015).

A. Colom, E. Derivery, S. Soleimanpour, C. Tomba, M. D. Molin, N. Sakai, M. González-Gaitán, S. Matile, A. Roux, A fluorescent membrane tension probe. *Nat Chem* **10**, 1118–1125 (2018).

C. Roffay, G. Molinard, K. Kim, M. Urbanska, V. Andrade, V. Barbarasa, P. Nowak, V. Mercier, J. García-Calvo, S. Matile, R. Loewith, A. Echard, J. Guck, M. Lenz, A. Roux, Passive coupling of membrane tension and cell volume during active response of cells to osmosis. *Proc Natl Acad Sci U S A* **118** (2021).

A. Bhattacharya, M. Agarwal, R. Mukherjee, P. Sen, D. K. Sinha, 3D micro-environment regulates NF-κβ dependent adhesion to induce monocyte differentiation. *Cell Death Dis* **9**, 914 (2018).

G. Kustermans, J. El Benna, J. Piette, S. Legrand-Poels, Perturbation of actin dynamics induces NF-kappaB activation in myelomonocytic cells through an NADPH oxidase-dependent pathway. *Biochem J* **387**, 531–40 (2005).

M. Agarwal, P. Biswas, A. Bhattacharya, D. K. Sinha, Reactive oxygen species-mediated cytoplasmic stiffening impairs the phagocytic ability of the macrophage. *J Cell Sci* **133** (2020).

V. H. Guaiquil, J. C. Vera, D. W. Golde, Mechanism of Vitamin C Inhibition of Cell Death Induced by Oxidative Stress in Glutathione-depleted HL-60 Cells. *Journal of Biological Chemistry* **276**, 40955–40961 (2001).

D. Ray, D. K. Sinha, Dynamic crosstalk between cytoskeletal filaments regulates dorsoventral cytoplasmic mechanics. *J Cell Sci* **138** (2025).

D. F. Legler, O. Micheau, M.-A. Doucey, J. Tschopp, C. Bron, Recruitment of TNF Receptor 1 to Lipid Rafts Is Essential for TNFα-Mediated NF-κB Activation. *Immunity* **18**, 655–664 (2003).

B. Sinha, D. Köster, R. Ruez, P. Gonnord, M. Bastiani, D. Abankwa, R. V. Stan, G. Butler-Browne, B. Vedie, L. Johannes, N. Morone, R. G. Parton, G. Raposo, P. Sens, C. Lamaze, P. Nassoy, Cells Respond to Mechanical Stress by Rapid Disassembly of Caveolae. *Cell* **144**, 402–413 (2011).

S. R. Hubbard, W. T. Miller, Receptor tyrosine kinases: mechanisms of activation and signaling. *Curr Opin Cell Biol* **19**, 117–23 (2007).

X. Su, J. A. Ditlev, E. Hui, W. Xing, S. Banjade, J. Okrut, D. S. King, J. Taunton, M. K. Rosen, R. D. Vale, Phase separation of signaling molecules promotes T cell receptor signal transduction. *Science (1979)* **352**, 595–599 (2016).

A. Burt, C. K. Cassidy, P. Ames, M. Bacia-Verloop, M. Baulard, K. Huard, Z. Luthey-Schulten, A. Desfosses, P. J. Stansfeld, W. Margolin, J. S. Parkinson, I. Gutsche, Complete structure of the chemosensory array core signalling unit in an E. coli minicell strain. *Nat Commun* **11**, 743 (2020).

A. K. Lewis, C. C. Valley, J. N. Sachs, TNFR1 signaling is associated with backbone conformational changes of receptor dimers consistent with overactivation in the R92Q TRAPS mutant. *Biochemistry* **51**, 6545–6555 (2012).

C. C. Valley, A. K. Lewis, D. J. Mudaliar, J. D. Perlmutter, A. R. Braun, C. B. Karim, D. D. Thomas, J. R. Brody, J. N. Sachs, Tumor Necrosis Factor-related Apoptosis-inducing Ligand (TRAIL) Induces Death Receptor 5 Networks That Are Highly Organized. *Journal of Biological Chemistry* **287**, 21265–21278 (2012).

H. Chakraborty, A. Chattopadhyay, Excitements and challenges in GPCR oligomerization: Molecular insight from FRET. *ACS Chem Neurosci* **6**, 199–206 (2015).

C. A. Coomer, I. Carlon-Andres, M. Iliopoulou, M. L. Dustin, E. B. Compeer, A. A. Compton, S. Padilla-Parra, Single-cell glycolytic activity regulates membrane tension and HIV-1 fusion. *PLoS Pathog* **16**, e1008359 (2020).

A. Biswas, P. Kashyap, S. Datta, T. Sengupta, B. Sinha, Cholesterol Depletion by MβCD Enhances Cell Membrane Tension and Its Variations-Reducing Integrity. *Biophys J* **116**, 1456–1468 (2019).

F. Christian, E. Smith, R. Carmody, The Regulation of NF-κB Subunits by Phosphorylation. *Cells* **5**, 12 (2016).

Y. Teijeiro-Gonzalez, A. Crnjar, A. J. Beavil, R. L. Beavil, J. Nedbal, A. Le Marois, C. Molteni, K. Suhling, Time-Resolved Fluorescence Anisotropy and Molecular Dynamics Analysis of a Novel GFP Homo-FRET Dimer. *Biophys J* **120**, 254–269 (2021).

T. Mandal, A. Biswas, T. Ghosh, S. Manikandan, A. Kundu, A. Banerjee, D. Mitra, B. Sinha, Mechano-regulation by clathrin pit-formation and passive cholesterol-dependent tubules during de-adhesion. *Cell Mol Life Sci* **81**, 43 (2024).

A. Biswas, A. Alex, B. Sinha, Mapping Cell Membrane Fluctuations Reveals Their Active Regulation and Transient Heterogeneities. *Biophys J* **113**, 1768–1781 (2017).

A. Mascret, H. Mouhsine, G. Attia, D. Cabrera, M. Benchekroun, P. Gizzi, C. Zerrouki, N. Fourati, J.-F. Zagury, M. S.-I. Veitía, M. Port, New contributions to the drug profile of TNFα inhibitor SPD304: Affinity, selectivity and ADMET considerations. *Eur J Pharmacol* 907, 174285 (2021).

M. M. He, A. S. Smith, J. D. Oslob, W. M. Flanagan, A. C. Braisted, A. Whitty, M. T. Cancilla, J. Wang, A. A. Lugovskoy, J. C. Yoburn, A. D. Fung, G. Farrington, J. K. Eldredge, E. S. Day, L. A. Cruz, T. G. Cachero, S. K. Miller, J. E. Friedman, I. C. Choong, B. C. Cunningham, Small-Molecule Inhibition of TNF-α. *Science (1979)* 310, 1022–1025 (2005).

P. H. Carter, P. A. Scherle, J. A. Muckelbauer, M. E. Voss, R.-Q. Liu, L. A. Thompson, A. J. Tebben, K. A. Solomon, Y. C. Lo, Z. Li, P. Strzemienski, G. Yang, N. Falahatpisheh, M. Xu, Z. Wu, N. A. Farrow, K. Ramnarayan, J. Wang, D. Rideout, V. Yalamoori, P. Domaille, D. J. Underwood, J. M. Trzaskos, S. M. Friedman, R. C. Newton, C. P. Decicco, Photochemically enhanced binding of small molecules to the tumor necrosis factor receptor-1 inhibits the binding of TNF-α. *Proceedings of the National Academy of Sciences* 98, 11879–11884 (2001).

J. O'Connell, J. Porter, B. Kroeplien, T. Norman, S. Rapecki, R. Davis, D. McMillan, T. Arakaki, A. Burgin, D. Fox III, T. Ceska, F. Lecomte, A. Maloney, A. Vugler, B. Carrington, B. P. Cossins, T. Bourne, A. Lawson, Small molecules that inhibit TNF signalling by stabilising an asymmetric form of the trimer. *Nat Commun* 10, 5795 (2019).

R. Murali, X. Cheng, A. Berezov, X. Du, A. Schön, E. Freire, X. Xu, Y. H. Chen, M. I. Greene, Disabling TNF receptor signaling by induced conformational perturbation of tryptophan-107. *Proceedings of the National Academy of Sciences* 102, 10970–10975 (2005).

R. K. Rowe, J. L. Harrison, H. Zhang, A. D. Bachstetter, D. P. Hesson, B. F. O'Hara, M. I. Greene, J. Lifshitz, Novel TNF receptor-1 inhibitors identified as potential therapeutic candidates for traumatic brain injury. *J Neuroinflammation* 15, 154 (2018).

F. Mancini, C. M. Toro, M. Mabilia, M. Giannangeli, M. Pinza, C. Milanese, Inhibition of tumor necrosis factor-α (TNF-α)/ TNF-α receptor binding by structural analogues of suramin§§Abbreviations: TNF-α, tumor necrosis factor-α; and MC/EM, MonteCarlo/energy minimization. *Biochem Pharmacol* 58, 851–859 (1999).

R. Alzani, A. Corti, L. Grazioli, E. Cozzi, P. Ghezzi, F. Marcucci, Suramin induces deoligomerization of human tumor necrosis factor alpha. *Journal of Biological Chemistry* 268, 12526–12529 (1993).

Q.-L. Hu, S. H. Liang, Novel Cyclic Peptides Inhibiting Tumor Necrosis Factor Receptor 1 Activity. *ACS Med Chem Lett* 16, 363–365 (2025).

Acknowledgments

We express our gratitude to the Central Scientific Services (CSS) of the Indian Association for the Cultivation of Science (IACS), Kolkata, for providing us with access to instrumental facilities. Special thanks to Mrs. Debapriya Ghatak, Mr. Chanchal Kumar Das, and Mr. Gopal Krishna Manna for their invaluable assistance with confocal microscopy, FACS, and graphical illustration, respectively. We are indebted to Prof. Maria Vartiainen (University of Helsinki, Finland) for generously gifting us with the GFP-GFP (2GFP) plasmid. Our appreciation goes to Dr. Dipyaman Ganguly (Indian Institute of Chemical Biology, Kolkata) for graciously allowing us to utilize FACS and to his student, Ms. Shreya Roy, for assisting with flow cytometry data acquisition. We also extend our gratitude to Dr. Prosenjit Sen (IACS, Kolkata) for providing us with an essential cell line (THP-1). BS thanks Wellcome Trust/DBT India Alliance fellowship (Grant Number IA/I/13/1/500885) for the TIRF imaging. We acknowledge ChatGPT 3.5 for rephrasing our write-up for clarity. Finally, we thank Dr. Mahesh Agarwal for critically reading the manuscript and providing valuable suggestions, which greatly contributed to preparing this manuscript for publication. Furthermore, we acknowledge IACS, Kolkata, for providing intramural funds.

Funding:

SERB Core Research Grant, Department of Science and Technology, Ministry of Science and Technology CRG/2022/005356 (DKS)

Department of Biotechnology, Ministry of Science and Technology BT/PR6995/BRB/10/1140/2012 (DKS)

SERB Grant number SERB_CRG_2458 (BS)

CEFIPRA Grant number 6303-1 (BS)

Indian Association for the Cultivation of Science, Kolkata 700032, India (SJ, PR, PB, BBB, NN)

Council of Scientific and Industrial Research 09/080(1074)/2018-EMR-I (PR)

University Grants Commission 201610161681 (JD)

Author contributions: SJ and PR are co-first authors of this paper and contributed equally. DKS, BS, SJ, and PR designed the project and prepared the manuscript. SJ, PR, and JD conducted the experiments and analyzed the data. JD performed the IRM and TIRF imaging. PB was responsible for setting up and calibrating the HeLa-mEGFP and HeLa-2GFP fluorescence anisotropy measurements. BBB and NN contributed to data analysis. BS assisted in reviewing the manuscript.

Competing interests: The authors declare that they have no competing interests.

Data and materials availability: All data are available in the main text or the supplementary materials. Codes used in the manuscript are freely available online (https:/github.com/SubhamoyJana/TNFR1-Project).

979 **Figures**

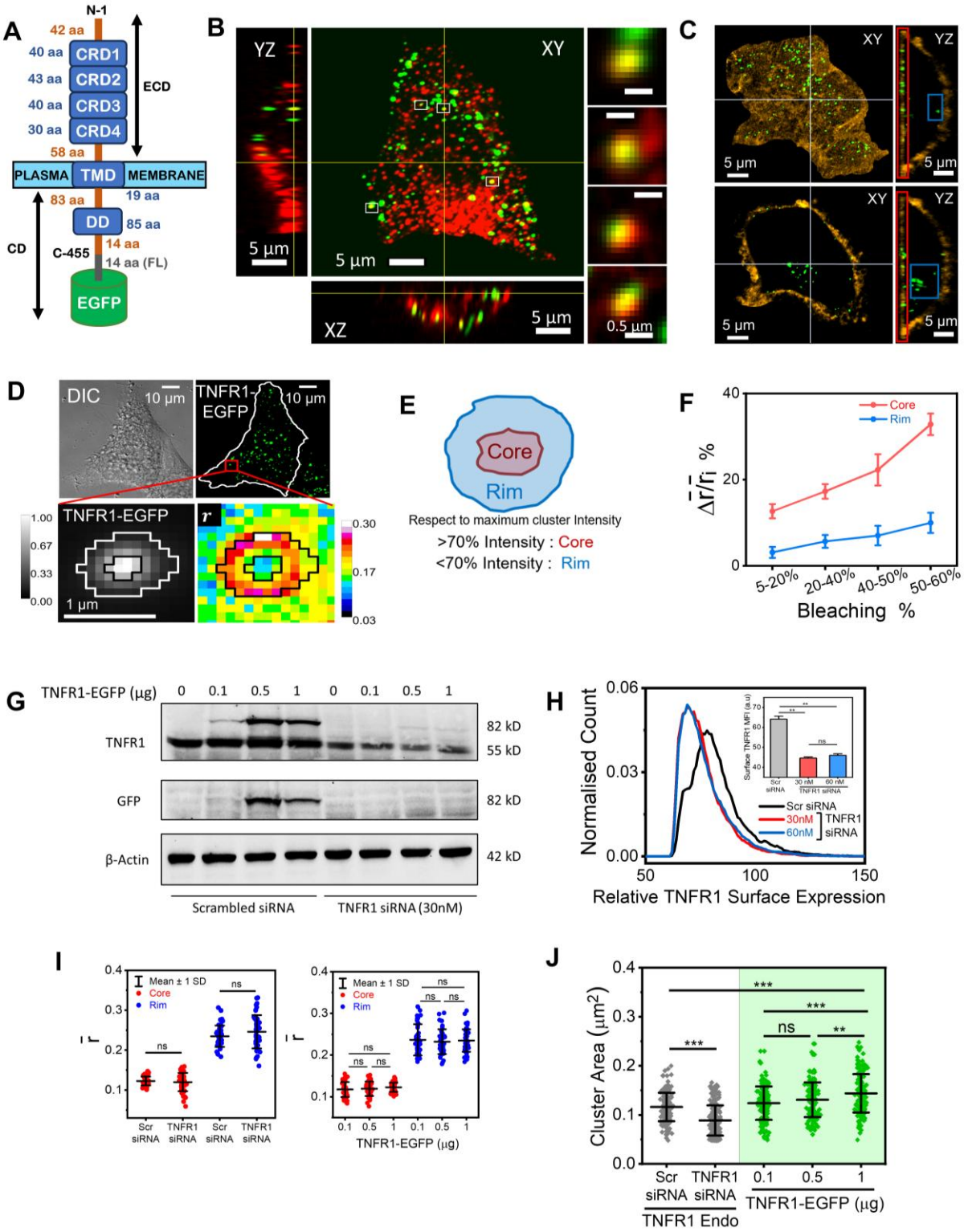

980
981

982 **Fig. 1. Homo-FRET–based mapping of intra-cluster receptor density (IRD) in TNFR1-EGFP**
983 **nanoclusters.**

984 (**A**) Schematic representation of the TNFR1-EGFP fusion construct showing the extracellular
985 domain (ECD), cysteine-rich domains (CRD1–4), transmembrane domain (TMD), cytoplasmic
986 domain (CD), and death domain (DD). An additional 14-amino-acid (aa) flexible linker (FL)
987 connects the C terminus of TNFR1 to EGFP. The amino acid lengths of individual domains are
988 indicated. (**B**) Confocal images of a HeLa cell expressing TNFR1-EGFP (green) and
989 immunostained with anti-TNFR1 antibody (red) in XY, YZ, and XZ planes. Merged and magnified
990 views of four representative clusters demonstrate colocalization between TNFR1-EGFP and
991 endogenous TNFR1. Images were processed to reduce noise by Gaussian averaging (radius = 1)
992 using ImageJ. (**C**) Representative confocal Airyscan images showing orthogonal sections (XY and
993 YZ) of a HeLa cell expressing TNFR1-EGFP (green) and labeled with CellMask Orange (orange)
994 to visualize the plasma membrane. Basal (z = 0; top) and mid-plane (z = 10; bottom) sections
995 highlight TNFR1 clusters localized at the plasma membrane (red box) and within the cytoplasm
996 (blue box). (**D**) Differential interference contrast (DIC; top left) and epifluorescence (top right)
997 images of a TNFR1-EGFP–expressing HeLa cell. Enlarged views display intensity (bottom left)
998 and fluorescence anisotropy (bottom right) maps of a representative TNFR1-EGFP cluster. (**E**)
999 Schematic illustration of a TNFR1 cluster depicting two sub-regions: a densely packed central core
1000 and a peripheral region of lower receptor density. (**F**) Percentage change in relative mean
1001 fluorescence anisotropy ($\Delta\bar{r}/\bar{r}_i$) plotted against the percentage of photobleaching for the core (red)
1002 and rim (blue) regions of TNFR1–EGFP clusters (n = 20) in live HeLa cells. Here, $\Delta\bar{r} = \bar{r}_f -$
1003 $\bar{r}_i$ where $\bar{r}_f$ and $\bar{r}_i$ represent post- and pre-bleach mean anisotropy, respectively. Data are means ±
1004 SEM from 3 cells each across two independent experiments. (**G**) Immunoblot analysis of HeLa
1005 cells transfected with scrambled or TNFR1 siRNA and co-transfected with increasing doses (0-1
1006 μg) of TNFR1-EGFP. Blots were probed with anti-TNFR1 and anti-GFP antibodies; β-Actin served
1007 as a loading control. Representative of two independent experiments. (**H**) Flow cytometric analysis
1008 of surface TNFR1 levels in control (scrambled siRNA) and TNFR1 siRNA–treated HeLa cells (30
1009 nM and 60 nM, day 4). The inset shows quantification of median fluorescence intensity (MFI).
1010 Representative of two independent experiments. (**I**) Mean fluorescence anisotropy ($\bar{r}$) of core (red)
1011 and rim (blue) regions of TNFR1-EGFP clusters (n = 45) in HeLa cells transfected with scrambled
1012 siRNA (Scr siRNA) or TNFR1 siRNA (left), and in cells overexpressing with increasing doses (0-
1013 1 μg) of TNFR1-EGFP (right). The data represent 3 cells each from three independent experiments.
1014 **(J)** Quantification of cluster area (μm^2) for endogenous TNFR1 clusters (n ≥ 170) in scrambled
1015 siRNA (Scr siRNA) and TNFR1 siRNA-treated HeLa cells (left, gray), and for exogenous TNFR1-
1016 EGFP clusters (n = 170) in cells expressing different doses (0-1 μg) of TNFR1-EGFP (right, green),

1017 acquired by confocal Airyscan imaging. The data represent 8 cells each from three independent
1018 experiments. Statistical significance between datasets was determined by one-way ANOVA (H-J)
1019 and is indicated in the figures as follows: $*P < 0.05$; $**P < 0.01$; $***P < 0.001$; ns, not significant.
1020 Scale bars, as indicated in the corresponding images.

1021
1022

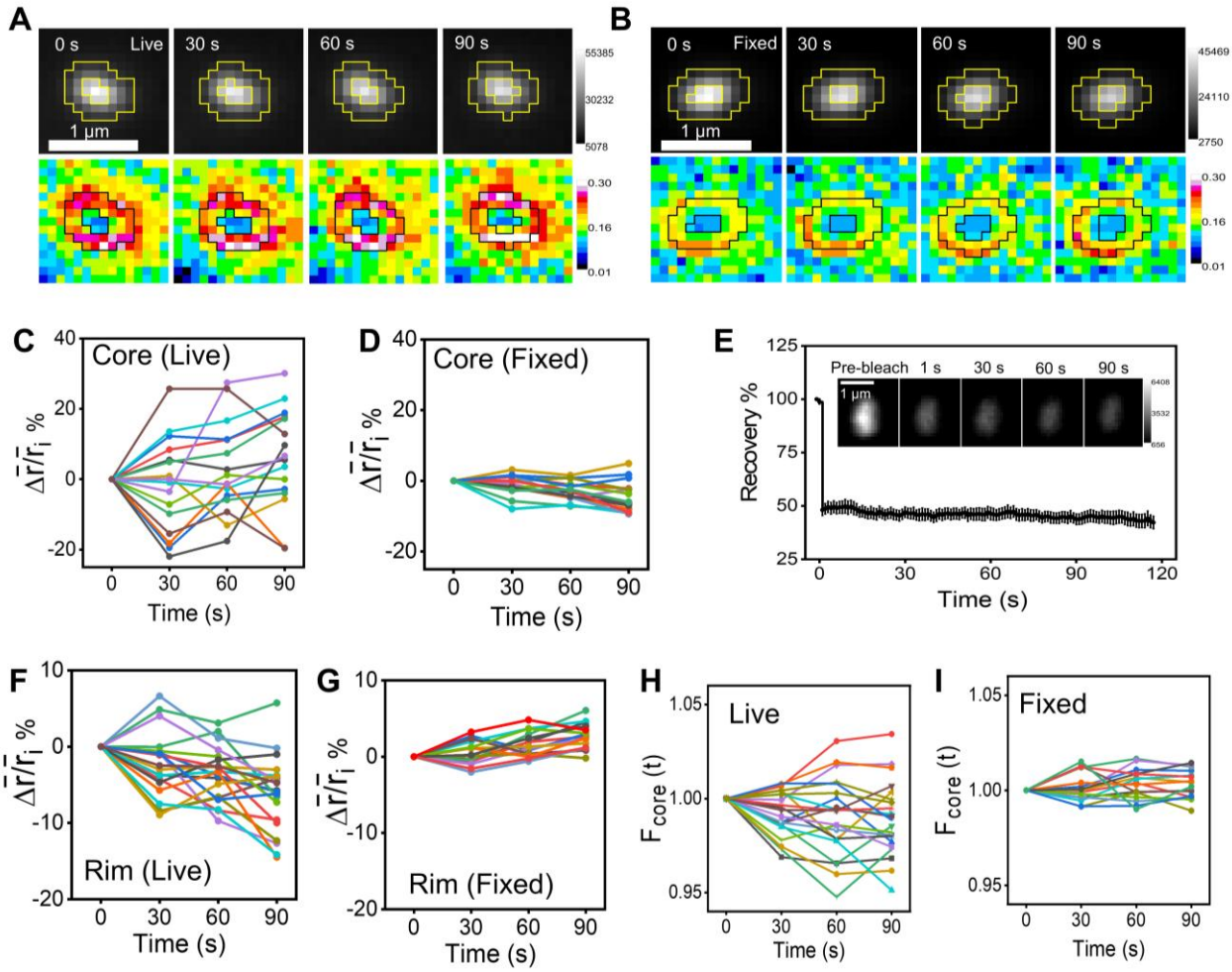

Fig. 2. Intra-cluster spatiotemporal dynamics of TNFR1-EGFP reveal spontaneous rearrangements of receptor molecules within clusters.

(**A** and **B**) Time-lapse intensity (top) and fluorescence anisotropy (bottom) maps of a single TNFR1-EGFP cluster in live (A) and fixed (B) HeLa cells monitored for 90 seconds. (**C** and **D**) Percentage change in relative mean fluorescence anisotropy ($\Delta\bar{r}/\bar{r}_i$), where $\Delta\bar{r} = \bar{r}(t) - \bar{r}_i$, for the core region plotted as a function of time (t) in live (C) and fixed (D) HeLa cells expressing TNFR1-EGFP, acquired over a 90-second time course. Here, $\bar{r}_i$ represents the initial mean anisotropy (t = 0), and $\bar{r}(t)$ represents the mean anisotropy at time t. The data represent 2 cells each from two independent experiments. (**E**) Fluorescence recovery of TNFR1-EGFP clusters after photobleaching, monitored up to 120 seconds at 1-second intervals using confocal microscopy. Data are shown as mean ± SEM (n = 10 clusters from 2 cells). Representative confocal images of a TNFR1-EGFP cluster before and after photobleaching are shown in the inset. Images were processed to reduce noise by Gaussian averaging (radius = 1) using ImageJ. (**F** and **G**) Percentage change in relative mean fluorescence anisotropy ($\Delta\bar{r}/\bar{r}_i$) of the rim region plotted as a function of time (t) in live (G) and fixed (H) HeLa cells expressing TNFR1-EGFP, acquired over a 90-second

1040 time course. (**H** and **I**) Temporal changes in the fractional fluorescence intensity of the core region,

1041 $F_{core}(t) = \frac{\frac{\bar{I}_{core}(t)}{(\bar{I}_{core}(t) + \bar{I}_{rim}(t))}}{\frac{\bar{I}_{core}(0)}{(\bar{I}_{core}(0) + \bar{I}_{rim}(0))}}$, for TNFR1-EGFP clusters in live (H) and fixed (I) HeLa cells, acquired

1042 over a 90-second time course. Here, $\bar{I}_{core}(t)$ and $\bar{I}_{rim}(t)$ represent mean fluorescence intensities in

1043 the core and rim regions at time t. Data in (C, D, F, G, H, I) represent n = 20 clusters from 2 cells

1044 each across two independent experiments. Scale bars are indicated in the corresponding images.

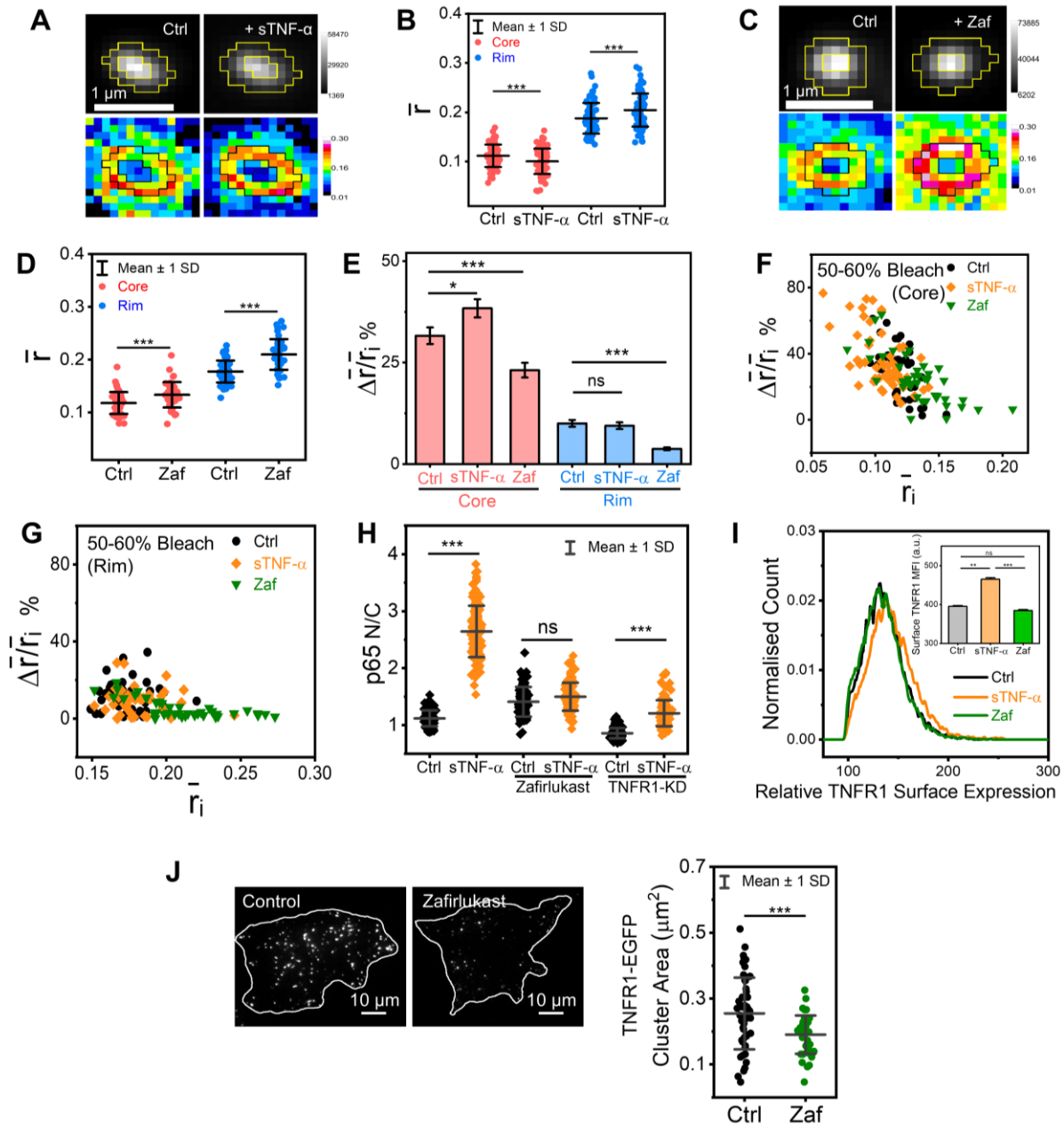

Fig. 3. Ligand binding and PLAD inhibition differentially remodel TNFR1 IRD and signaling. (**A**) Representative fluorescence intensity (top) and corresponding fluorescence anisotropy (bottom) maps of the same TNFR1-EGFP cluster in live HeLa cells before (Ctrl) and after sTNF-α stimulation (20 ng/mL, 5 min). (**B**) Mean fluorescence anisotropy ($\bar{r}$) of the core (red) and rim (blue) regions of the same TNFR1-EGFP clusters (n = 90) under control (Ctrl) and sTNF-α–treated conditions. The data represent 3 cells each from three independent experiments. (**C**) Representative fluorescence intensity (top) and corresponding fluorescence anisotropy (bottom) maps of a TNFR1-EGFP cluster in live HeLa cells before (Ctrl) and after zafirlukast (Zaf) treatment (100 μM, 1 h). (**D**) Mean fluorescence anisotropy ($\bar{r}$) of the core (red) and rim (blue) regions of TNFR1-EGFP

clusters (n = 50) under control (Ctrl) and zafirlukast-treated (Zaf) conditions. The data represent 3 cells each in three independent experiments. (**E**) Percentage change in relative mean fluorescence anisotropy ($\Delta\bar{r}/\bar{r}_i$) of the core (red) and rim (blue) regions of TNFR1-EGFP clusters (n ≥ 45) upon 50-60% photobleaching in control (Ctrl), sTNF-α, and zafirlukast-treated (Zaf) conditions. Here, $\Delta\bar{r} = \bar{r}_f - \bar{r}_i$ where $\bar{r}_f$ and $\bar{r}_i$ represent post- and pre-bleach mean anisotropy, respectively. The data represent 2 cells each in three independent experiments. (**F** and **G**) Scatter plots showing the relationship between percentage change in relative mean fluorescence anisotropy ($\Delta\bar{r}/\bar{r}_i$) and the initial mean anisotropy ($\bar{r}_i$) in the core (F) and rim (G) regions of TNFR1-EGFP clusters (n ≥ 45) upon 50-60% photobleaching under control (Ctrl), sTNF-α, and zafirlukast-treated (Zaf) conditions. The data represent 2 cells each in three independent experiments. (**H**) Quantification of nuclear-to-cytoplasmic (N/C) mean intensity ratio of endogenous NF-κB (p65) in control (Ctrl) and sTNF-α–stimulated (20 ng/mL, 30 min) HeLa cells under untreated, zafirlukast-treated (Zaf), and TNFR1-knockdown (TNFR1-KD) conditions. Each control group corresponds to its respective treatment. The data represent 35 cells per condition from three independent experiments. (**I**) Flow cytometric analysis of surface TNFR1 expression in control (Ctrl), sTNF-α (20 ng/mL, 30 min), and zafirlukast-treated (Zaf) HeLa cells. The quantification of the median fluorescence intensity (MFI) is shown in the inset. (**J**) Representative TIRF images of immobile TNFR1-EGFP clusters in untreated (Ctrl, left) and zafirlukast-treated (Zaf, right) HeLa cells, with quantification of cluster area (μm²) shown (Ctrl: n = 49 clusters; Zaf: n = 43 clusters). Data are presented as means ± SD from 2 cells each in three independent experiments. Statistical significance between datasets was determined by paired two-tailed Student's *t*-test (B), unpaired two-tailed Student's *t*-test (D and J), or one-way ANOVA (E, H, I) and is indicated in the figures as follows: ∗P < 0.05; ∗∗P < 0.01; ∗∗∗P < 0.001; ns, not significant. Scale bars are indicated in the corresponding images.

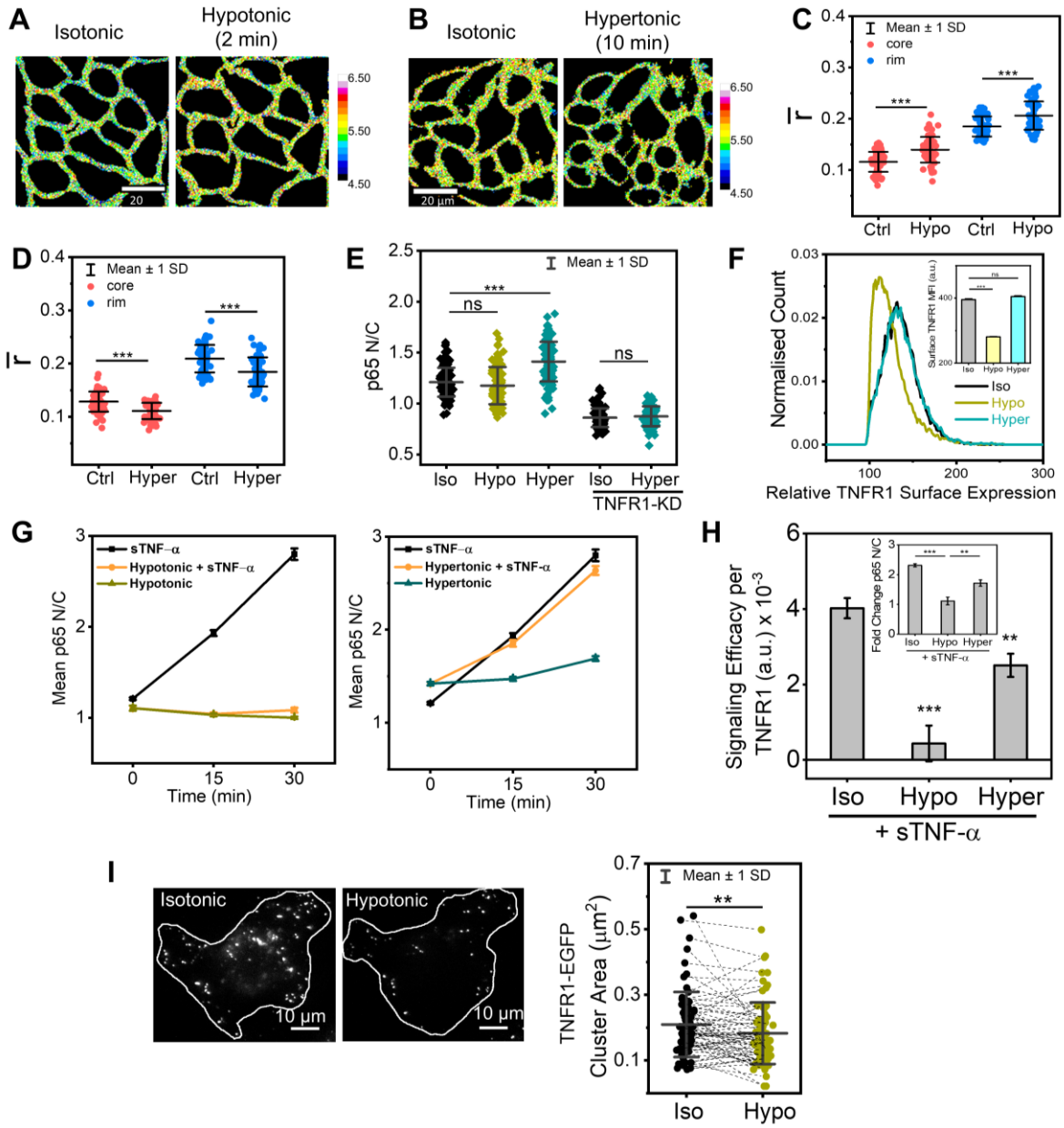

Fig. 4. Membrane tension regulates TNFR1 IRD and modulates signaling efficacy.

(**A** and **B**) Representative fluorescence lifetime maps of Flipper-TR (200 nM, 15 min) in HeLa cells subjected to (A) hypotonic (75% water, 2 min) and (B) hypertonic (150 mM mannitol, 10 min) shocks relative to the isotonic condition. (**C**) Mean fluorescence anisotropy ($\bar{r}$) of the core (red) and rim (blue) regions of TNFR1-EGFP clusters (n = 60) under hypotonic conditions (Hypo) compared to isotonic control (Ctrl). The data represent 5 cells each in three independent experiments. (**D**) Mean fluorescence anisotropy ($\bar{r}$) of the core (red) and rim (blue) regions of TNFR1-EGFP clusters (n = 60) under hypertonic conditions (Hyper) compared to isotonic control (Ctrl). The data represent

5 cells each in three independent experiments. (**E**) Nuclear-to-cytoplasmic (N/C) mean intensity ratio of endogenous NF-κB (p65) analyzed by immunostaining in HeLa cells subjected to isotonic (Iso), hypotonic (Hypo), or hypertonic (Hyper) conditions, in both control and TNFR1-knockdown (TNFR1-KD) cells. The data represent 35 cells each in three independent experiments. (**F**) Surface expression levels of endogenous TNFR1 in HeLa cells under isotonic (Iso), hypotonic (Hypo), and hypertonic (Hyper) conditions measured by flow cytometry. The quantification of the median fluorescence intensity (MFI) in each condition is shown in the inset. (**G**) Quantification of p65 N/C mean intensity ratio over 30 minutes following sTNF-α stimulation under hypotonic (left) and hypertonic (right) conditions compared to isotonic control. (**H**) Signaling efficacy of TNFR1 in HeLa cells subjected to isotonic (Iso), hypotonic (Hypo), and hypertonic (Hyper) shocks in response to sTNF-α. Signaling efficacy represents the N/C ratio change of p65 normalized to surface TNFR1 levels (ΔN/C p65 ratio / respective surface TNFR1 MFI). The inset shows fold change in p65 N/C ratio under each condition relative to corresponding unstimulated controls. Data represent means ± SD of 30 cells each in three independent experiments. (**I**) Representative TIRF images of TNFR1-EGFP–expressing HeLa cells before (left) and after (right) hypotonic shock. Quantification of TNFR1-EGFP cluster area (μm^2) of the same clusters ($n = 73$) before and after treatment is shown. Data represent means ± SD from 3 cells each in three independent experiments. Statistical significance between datasets was determined by unpaired two-tailed Student's *t*-test (C, D), one-way ANOVA (E, F, H), or paired two-tailed Student's *t*-test (I) and is indicated in the figures as follows: $*P < 0.05$; $**P < 0.01$; $***P < 0.001$; ns, not significant. Scale bars are indicated in the corresponding images.

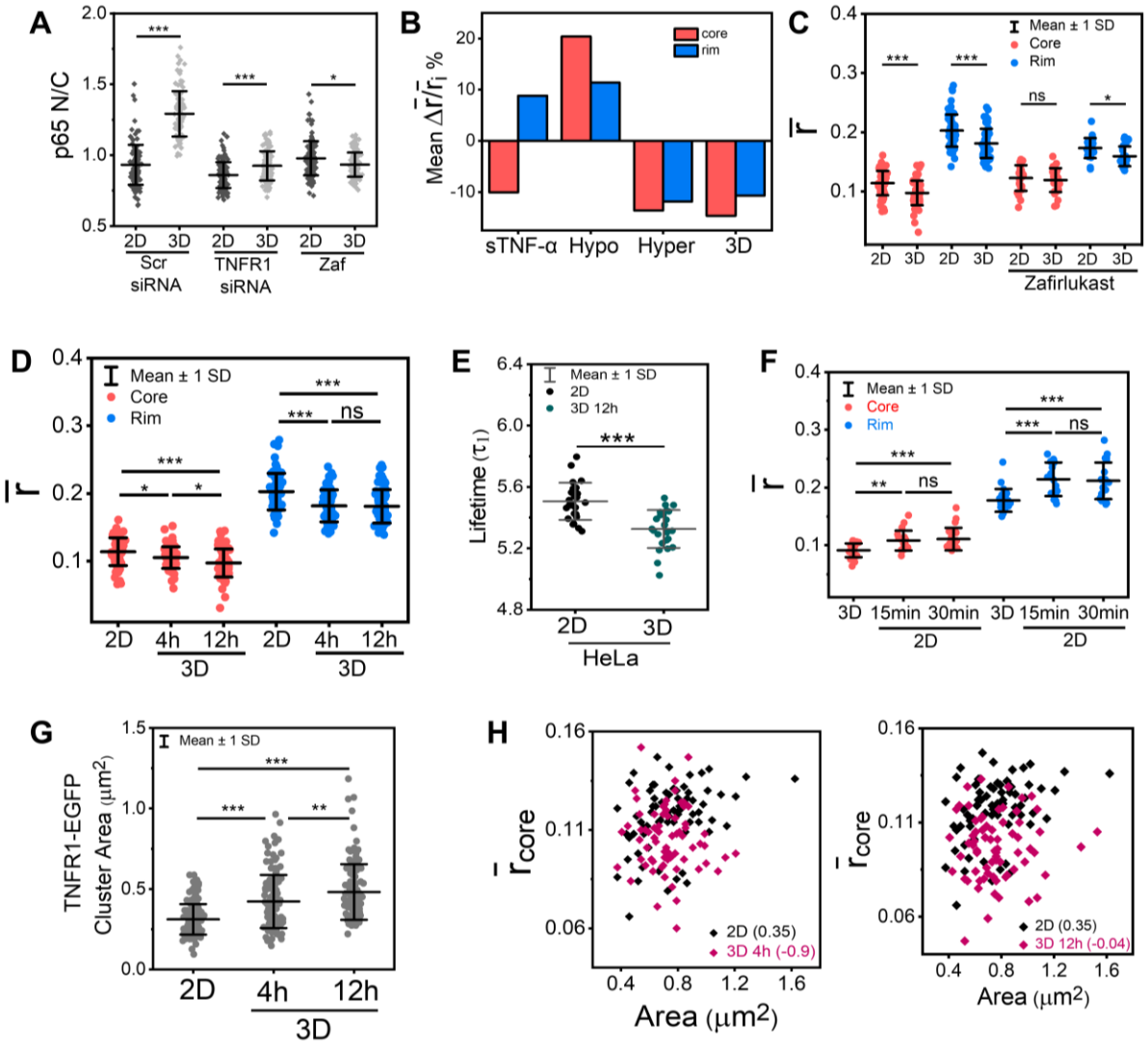

Fig. 5. 3D gel-like microenvironment induces ligand-independent TNFR1 signaling by modulating IRD.

(**A**) Nuclear-to-cytoplasmic (N/C) mean intensity ratio of endogenous NF-κB (p65) in HeLa cells cultured in 2D (control) or 3D (1% agarose gel cover, 12 h) under scrambled siRNA (Scr siRNA), TNFR1 siRNA, or zafirlukast-treated (Zaf) conditions, analyzed by immunostaining. The data represent 35 cells each in three independent experiments. (**B**) Percentage change in relative mean fluorescence anisotropy ($\Delta\bar{r}/\bar{r}_i$) of core (red) and rim (blue) regions of TNFR1-EGFP clusters (n = 60) in HeLa cells under sTNF-α treatment, hypotonic (Hypo), hypertonic (Hyper), and 3D conditions, normalized to their respective controls. Here, $\Delta\bar{r} = \bar{r}_f - \bar{r}_i$ where $\bar{r}_f$ and $\bar{r}_i$ represent the final and initial mean anisotropy for each treatment, respectively. The data represent 3 cells each in three independent experiments. (**C**) Mean fluorescence anisotropy ($\bar{r}$) of core (red) and rim (blue) regions of TNFR1-EGFP clusters in HeLa cells in 2D (control) or 3D under untreated (n =

60 clusters) or zafirlukast-treated (n = 25 clusters) conditions. The data represent 3 cells each in three independent experiments. (**D**) Mean fluorescence anisotropy ($\bar{r}$) of core (red) and rim (blue) regions of TNFR1-EGFP clusters (n = 70) during the transition from 2D to 3D culture after 4 h and 12 h of incubation. The data represent 3 cells each in three independent experiments. (**E**) Fluorescence lifetime (τ_1) of Flipper-TR in HeLa cells cultured in 2D or 3D medium. The data represent 8 cells each in three independent experiments. (**F**) Mean fluorescence anisotropy ($\bar{r}$) of core (red) and rim (blue) regions of TNFR1-EGFP clusters (n = 20) in HeLa cells transitioning from 3D to 2D culture after 15 min and 30 min of incubation. The data represent 2 cells each in two independent experiments. (**G**) Quantification of area (μm²) of TNFR1-EGFP clusters (n = 124) in HeLa cells in 2D (control) and 3D conditions after 4 h and 12 h of incubation, acquired by epifluorescence imaging. The data represent 5 cells each in three independent experiments. (**H**) Scatter plots of TNFR1-EGFP cluster area (μm²) versus mean fluorescence anisotropy of the core ($\bar{r}_{core}$) of the same TNFR1-EGFP clusters (n = 70) in HeLa cells cultured in 2D and 3D [4 h (left) and 12 h (right)]. Pearson's correlation coefficients are indicated for each condition. The data represent 3 cells each in three independent experiments. Statistical significance between datasets was determined by one-way ANOVA (A, D, F, G) or unpaired two-tailed Student's *t*-test (C, E) and is indicated in the figures as follows: $*P < 0.05$; $**P < 0.01$; $***P < 0.001$; ns, not significant. Scale bars are indicated in the corresponding images.

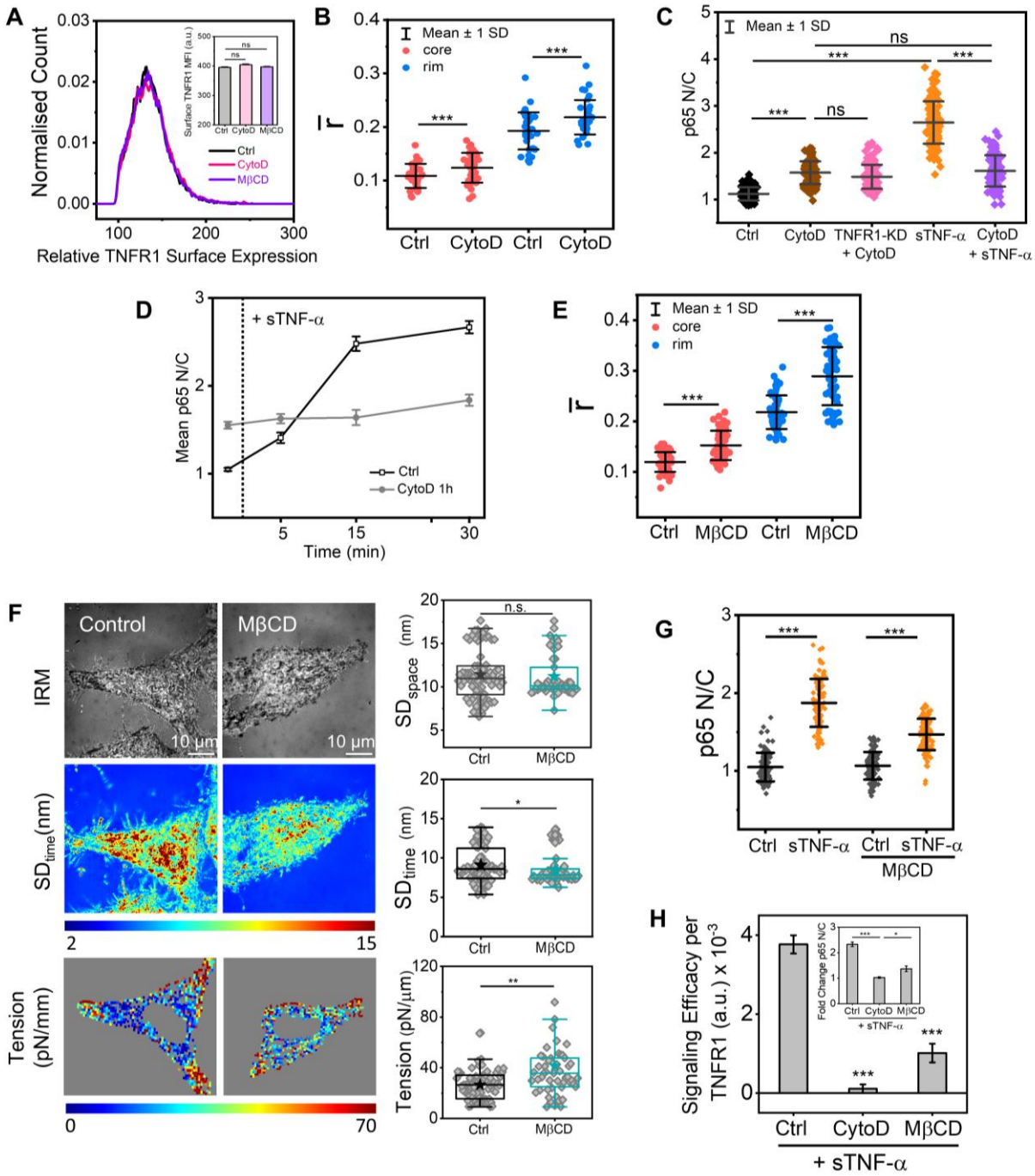

Fig. 6. Cytoskeletal and membrane perturbations reduce TNFR1 IRD and signaling efficacy. (**A**) Surface expression of endogenous TNFR1 in HeLa cells under control (Ctrl), cytochalasin D-treated (CytoD, 2 μM, 1 h), and methyl-β-cyclodextrin-treated (MβCD, 2 mM, 1 h) conditions, measured by flow cytometry. Median fluorescence intensity (MFI) is shown in the inset. (**B**) Mean fluorescence anisotropy ($\bar{r}$) of the core (red) and rim (blue) regions of TNFR1-EGFP clusters (n = 34) in control (Ctrl) and CytoD-treated HeLa cells. The data represent 2 cells across two

independent experiments. (**C**) Nuclear-to-cytoplasmic (N/C) mean intensity ratio of NF-κB (p65) in control (Ctrl), CytoD-treated, TNFR1-knockdown (TNFR1-KD), and sTNF-α-stimulated HeLa cells, analyzed by immunostaining. The data represent 35 cells each in three independent experiments. (**D**) Temporal changes in the N/C ratio of p65 in control (Ctrl) and CytoD-treated HeLa cells in response to sTNF-α, monitored for 30 minutes. Data are presented as means ± SEM of 35 cells in three independent experiments. (**E**) Mean fluorescence anisotropy ($\bar{r}$) of the core (red) and rim (blue) regions of TNFR1-EGFP clusters (n = 64) in control (Ctrl) and MβCD-treated HeLa cells. The data represent 3 cells across three independent experiments. (**F**) Representative Interference Reflection Microscopy (IRM) images (top), corresponding SD_{time} maps (middle), and membrane tension maps (bottom) of control (Ctrl) and MβCD-treated HeLa cells. Quantification of SD_{time} (nm) and membrane tension (pN/μm) is shown (Ctrl: n = 79 cells; MβCD: n = 57 cells). Data are representative of three independent experiments. (**G**) N/C mean intensity ratio of NF-κB (p65) in control (Ctrl) and MβCD-treated HeLa cells with or without sTNF-α stimulation. The data represent 35 cells each in three independent experiments. (**H**) TNFR1 signaling efficacy, defined as the change in p65 N/C ratio normalized to surface TNFR1 levels (MFI), in control, CytoD, and MβCD-treated HeLa cells in response to sTNF-α. The fold change of p65 N/C, normalized to its respective basal levels, is shown in the inset. Data are presented as means ± SD of 30 cells each in three independent experiments. Statistical significance between datasets was determined by one-way ANOVA (A, C, G, H) or unpaired two-tailed Student's *t*-test (B, E) and is indicated in the figures as follows: $*P < 0.05$; $**P < 0.01$; $***P < 0.001$; ns, not significant. Scale bars are indicated in the corresponding images.

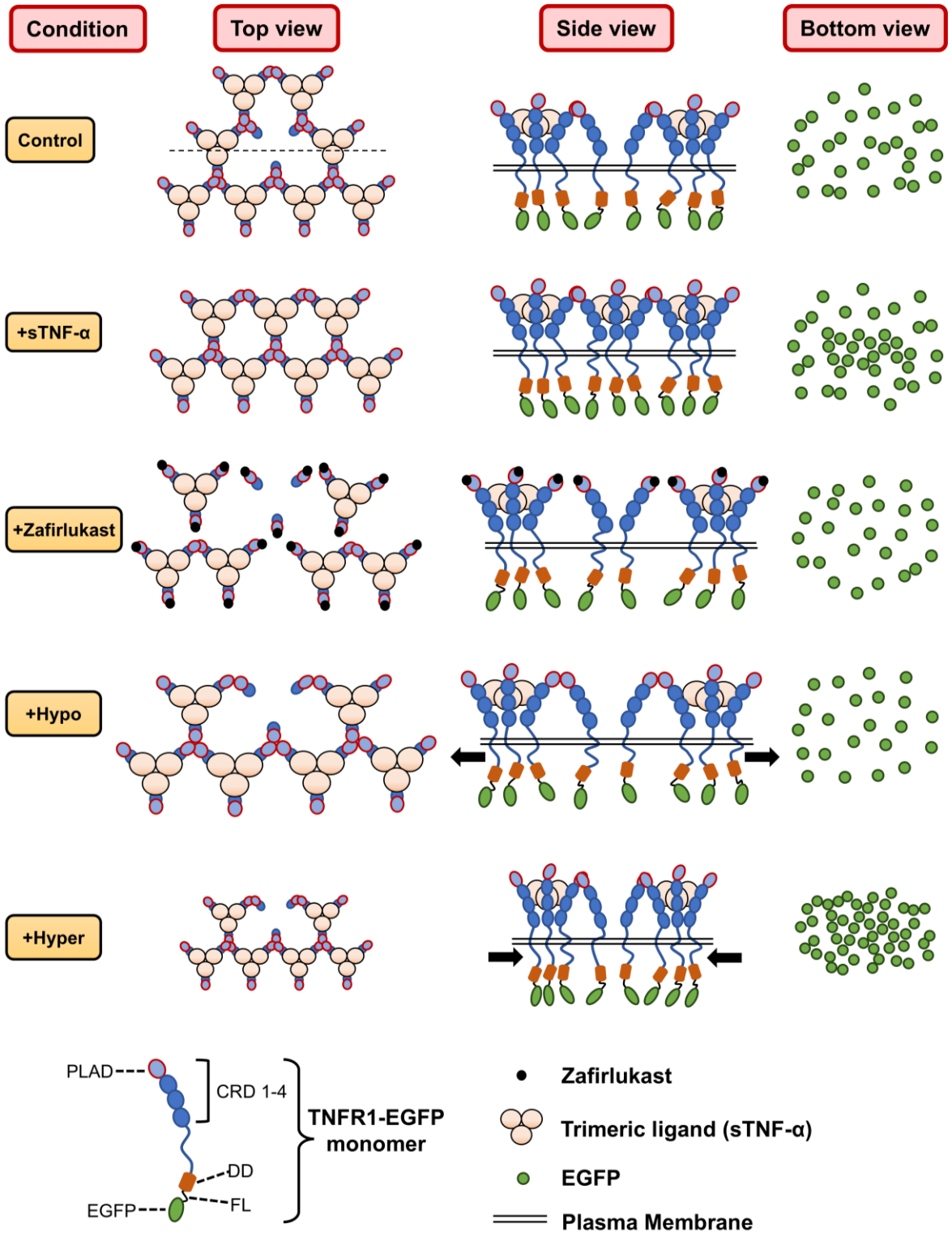

Fig. 7. Schematic model of TNFR1 cluster organization governed by ligand-receptor and receptor-receptor interactions.

Top (extracellular), side (lateral), and bottom (cytoplasmic) views illustrate the proposed schematic arrangement of TNFR1–EGFP molecules within a cluster under different conditions. In the native

1186 (control) state, TNFR1 exists in pre-assembled clusters formed through ligand–receptor and
1187 PLAD–PLAD interactions, with a few unoccupied binding sites in the cluster core. Upon ligand
1188 stimulation, these vacant sites become occupied, resulting in increased intermolecular proximity
1189 (higher IRD) in the core and reduced IRD at the rim, as visualized from the cytoplasmic (bottom)
1190 view. Zafirlukast treatment disrupts PLAD–PLAD interactions, leading to decreased IRD in both
1191 the core and rim regions. Hypotonic stress increases membrane tension, expanding intermolecular
1192 distances and reducing IRD throughout the cluster. Conversely, hypertonic stress reduces
1193 membrane tension, promoting molecular proximity and increasing IRD across both regions. PLAD,
1194 pre-ligand assembly domain; CRD, cysteine-rich domain; DD, death domain; FL, flexible linker.
1195